
Research Article: New Research | Sensory and Motor Systems

Distinct Neural Properties in the Low Frequency Region of the Chicken Cochlear Nucleus Magnocellularis

Distinct neural features of the chicken caudal NM

Xiaoyu Wang^{1,2}, Hui Hong³, David H. Brown^{2,4}, Jason Tait Sanchez^{3,5,6} and Yuan Wang^{1,2}

¹*Department of Biomedical Sciences, Florida State University College of Medicine, Tallahassee, FL 32306*

²*Program in Neuroscience, Florida State University, Tallahassee, FL 32306*

³*Roxelyn and Richard Pepper Department of Communication Sciences and Disorders, Northwestern University, Evanston, IL 60208*

⁴*Department of Psychology, Florida State University, Tallahassee, FL 32306*

⁵*Department of Neurobiology, Northwestern University, Evanston, IL 60208*

⁶*The Hugh Knowles Hearing Research Center, Northwestern University, Evanston, IL 60208*

DOI: 10.1523/ENEURO.0016-17.2017

Received: 12 January 2017

Revised: 17 February 2017

Accepted: 5 March 2017

Published: 4 April 2017

Author contributions: X.W., H.H., J.T.S., and Y.W. designed research; X.W., H.H., and D.H.B. performed research; X.W., H.H., D.H.B., and Y.W. analyzed data; X.W., H.H., D.H.B., J.T.S., and Y.W. wrote the paper.

Funding: HHS | NIH | National Institute on Deafness and Other Communication Disorders (NIDCD)
100000055
DC013074

Funding: HHS | NIH | National Institute on Deafness and Other Communication Disorders (NIDCD)
100000055
DC013841

Funding: Hugh Knowles Hearing research center

The authors declare no competing financial interests.

HHS | NIH | National Institute on Deafness and Other Communication Disorders (NIDCD) [DC013074].

Correspondence to: Yuan Wang, Ph.D., Department of Biomedical Sciences, Florida State University, 1115 West Call Street, Tallahassee, FL 32306. Phone: (850) 645-4934; email: yuan.wang@med.fsu.edu or Jason Tait Sanchez, Ph.D., Frances Searle Building, 2240 Campus Drive, Northwestern University, Evanston, IL 60208. Phone: 847 491-4648; email: jason.sanchez@northwestern.edu

Cite as: eNeuro 2017; 10.1523/ENEURO.0016-17.2017

Alerts: Sign up at eneuro.org/alerts to receive customized email alerts when the fully formatted version of this article is published.

Accepted manuscripts are peer-reviewed but have not been through the copyediting, formatting, or proofreading process.

This is an open-access article distributed under the terms of the Creative Commons Attribution 4.0 International (<http://creativecommons.org/licenses/by/4.0>), which permits unrestricted use, distribution and reproduction in any medium provided that the original work is properly attributed.

1 **Distinct neural properties in the low frequency region of the chicken cochlear**
2 **nucleus magnocellularis**

3
4 Xiaoyu Wang^{1,2}, Hui Hong³, David H. Brown^{2,4}, Jason Tait Sanchez^{3,5,6,*}, and Yuan Wang^{1,2,*}

5
6 1. Department of Biomedical Sciences, Florida State University College of Medicine,
7 Tallahassee, FL 32306

8 2. Program in Neuroscience, Florida State University, Tallahassee, FL 32306

9 3. Roxelyn and Richard Pepper Department of Communication Sciences and Disorders,
10 Northwestern University, Evanston, IL 60208

11 4. Department of Psychology, Florida State University, Tallahassee, FL 32306

12 5. Department of Neurobiology, Northwestern University, Evanston, IL 60208

13 6. The Hugh Knowles Hearing Research Center, Northwestern University, Evanston, IL 60208

14
15 **Abbreviated title:** Distinct neural features of the chicken caudal NM

16 **Correspondence to:**

17 Yuan Wang, Ph.D.

18 Department of Biomedical Sciences, Florida State University

19 1115 West Call Street, Tallahassee, FL 32306

20 Phone: (850) 645-4934; email: yuan.wang@med.fsu.edu

21 &

22 Jason Tait Sanchez, Ph.D.

23 Frances Searle Building, 2240 Campus Drive

24 Northwestern University, Evanston, IL 60208

25 Phone: (847) 491-4648; email: jason.sanchez@northwestern.edu

26

27 64 pages; 12 figures; 2 tables

28 237 words in Abstract; 82 words in Significance Statement; 536 words in Introduction; 2021

29 words in Discussion

30

31

32

33 **Acknowledgements:** The authors would like to thank Richard L. Hyson (Florida State
34 University) and Edwin W Rubel (University of Washington) for valuable comments to this
35 manuscript. This study is supported by National Institute on Deafness and Other Communication
36 Disorders (NIDCD): DC013074 (YW) and DC013841 (JTS), and the Hughes Knowles Hearing
37 Research Center (JTS and YW). The authors declare no competing financial interests.

38 **Abstract**

39 Topography in the avian cochlear nucleus magnocellularis (NM) is represented as gradually
40 increasing characteristic frequency (CF) along the caudolateral to rostromedial axis. In this
41 study, we characterized the organization and cell biophysics of the caudolateral NM (NMc) in
42 chickens (*Gallus gallus domesticus*). Examination of cellular and dendritic architecture first
43 revealed that NMc contains small neurons and extensive dendritic processes, in contrast to
44 adendritic, large neurons located more rostromedially. Individual dye-filling study further
45 demonstrated that NMc is divided into two subregions, with NMc2 neurons having larger and
46 more complex dendritic fields than NMc1. Axonal tract tracing studies confirmed that NMc1 and
47 NMc2 neurons receive afferent inputs from the auditory nerve and the superior olivary nucleus,
48 similar to the adendritic NM. However, the auditory axons synapse with NMc neurons via small
49 bouton-like terminals, unlike the large end-bulb synapses on adendritic NM neurons.
50 Immunocytochemistry demonstrated that most NMc2 neurons express cholecystokinin but not
51 calretinin, distinct from NMc1 and adendritic NM neurons that are cholecystokinin-negative and
52 mostly calretinin-positive. Finally, whole-cell current clamp recordings revealed that NMc
53 neurons require significantly lower threshold current for action potential generation than
54 adendritic NM neurons. Moreover, in contrast to adendritic NM neurons that generate a single
55 onset action potential, NMc neurons generate multiple action potentials to suprathreshold
56 sustained depolarization. Taken together, our data indicate that NMc contains multiple neuron
57 types that are structurally, connectively, molecularly, and physiologically different from
58 traditionally defined NM neurons, emphasizing specialized neural properties for processing low
59 frequency sounds.

60 **Significance Statement**

61 Low frequency sounds are important for auditory perception and scene analysis including speech
62 recognition. Using an avian model sensitive to low frequency hearing including infrasound, we
63 characterized neuronal properties of a primary cochlear nucleus. We found that the neurons
64 located at the low frequency end of the tonotopic axis develop unique structural, synaptic,
65 biochemical and physiological features, distinct from well-characterized neurons processing
66 sounds of higher frequencies. These findings provide fundamental knowledge towards
67 understanding the properties of low frequency processing in the brain.

68

69 **Introduction**

70 Topographic organization is a salient feature of sensory systems in the vertebrate brain (Moerel
71 et al., 2014; Kaneko and Ye, 2015). In the auditory system, topography manifests as tonotopy,
72 defined as the spatial representation of sound frequency in the brain. For optimally performing
73 auditory tasks across sound frequencies, auditory neurons develop gradients of structural,
74 synaptic, and intrinsic properties along the tonotopic axis. In the auditory brainstem, frequency-
75 specific neuronal processing is tuned by tonotopic gradients of ion channel expression (von Hehn
76 et al., 2004; Leao et al., 2006; Gazula et al., 2010), synaptic transmission and depression (Köppl,
77 1994; Fukui and Ohmori, 2004; Slee et al., 2010; Oline and Burger, 2014) and inhibitory kinetics
78 (Tang et al., 2011; Wang et al., 2012).

79 In addition to the mechanisms associated with tonotopic gradients, studies in birds
80 provide evidence that the auditory system may adopt a number of novel properties for processing
81 low frequency sounds. Birds can hear sound frequencies as low as 2-10 Hz as demonstrated by
82 behavior tests (Hill et al., 2014) and single-unit physiological recordings (Warchol and Dallos,
83 1990). The avian nucleus magnocellularis (NM) is a primary cochlear nucleus and is analogous
84 to the mammalian anteroventral cochlear nucleus (Ryugo and Parks, 2003). In chickens and
85 owls, NM neurons display gradually increasing characteristic frequency (CF) from the
86 caudolateral to rostromedial extent (Rubel and Parks, 1975; Takahashi and Konishi, 1988). NM
87 neurons typically have few, short dendrites and receive excitatory inputs from the auditory nerve
88 through large synapses on their cell bodies, the so-called End Bulbs of Held (Cajal, 1909; Boord
89 and Rasmussen, 1963; Parks and Rubel, 1978; Rubel and Fritzsche, 2002). These structural
90 specializations are thought to be important for processing temporally locked excitation and
91 computing the location of sound source stimuli (Sullivan and Konishi, 1984; Oertel, 1985; Carr

92 and Konishi, 1990; Warchol and Dallos, 1990; Trussell, 1999). Neurons located in the most
93 caudolateral NM, however, appear devoid of End Bulbs, favoring multiple traditional bouton
94 synaptic specializations (Takahashi and Konishi, 1988; Köppl, 1994; Köppl and Carr, 1997;
95 Fukui and Ohmori, 2004). NM neurons in this region have smaller cell bodies and possess
96 extensive dendrites, in contrast to the typical adendritic morphology of higher CF neurons
97 (Boord and Rasmussen, 1963). Regardless of these structural differences, *in vivo* recording
98 studies demonstrate that NM neurons with low CFs perform temporal phase locking as accurate
99 as, if not better, than neurons with higher CFs (Warchol and Dallos, 1990; Fukui et al., 2006,
100 Oline et al., 2016). These studies suggest that the auditory system may develop distinct neuronal
101 properties for similar function in temporal processing at different frequencies.

102 The current study provides a systematic characterization of the organization,
103 connectivity, and neural properties of the caudolateral NM distinct from higher frequency
104 regions of the nucleus. Using a combination of neuroanatomical and physiological approaches,
105 we identify two caudolateral NM subregions, NMc1 and NMc2. NMc1 and NMc2 are distinct
106 from adendritic NM neurons in the expression of a neuropeptide and calcium-binding proteins, in
107 addition to their extensive dendritic development and bouton-like synapses with the auditory
108 axons. Importantly, NMc1 and NMc2 neurons display the ability of generating multiple action
109 potentials following sustained current injections and show heterogeneity in their spiking activity,
110 features not found in adendritic NM neurons.

111

112 **Materials and Methods**

113 **Animals**

114 White leghorn chicken embryos and hatchlings (*Gallus gallus domesticus*) of either sex were

115 used. Chickens take approximately 21 days to hatch. We used chickens from late embryonic (E)
116 stage at E19 up to two weeks post-hatch (P14). At this age range, near-mature hearing ability is
117 established (Saunders et al., 1974; Rebillard and Rubel, 1981) and NM neurons have obtained
118 mature-like morphology and physiology (Jhaveri and Morest, 1982; Burger et al., 2005b;
119 Sanchez et al., 2010; Sanchez et al., 2012a; Sanchez et al., 2015a). Eggs for anatomical studies
120 were obtained from the Charles River Laboratories (Wilmington, MA) and incubated in a Florida
121 State University vivarium. Eggs for electrophysiological studies were obtained from Sunnyside
122 Farms, Inc. (Beaver Dam, WI) and incubated in the central auditory physiology laboratory at
123 Northwestern University. All procedures were approved by the Florida State University and
124 Northwestern University Institutional Animal Care and Use Committees, and carried out in
125 accordance with the National Institutes of Health Guide for the Care and Use of Laboratory
126 Animals.

127 **Immunohistochemistry**

128 Chicken hatchlings (P2-14; n=21) were transcardially perfused with 0.9% saline followed by 4%
129 paraformaldehyde in 0.1 M phosphate buffer (PB). The brains were removed from the skull,
130 post-fixed overnight in 4% paraformaldehyde, and transferred to 30% sucrose in PB with 0.02%
131 sodium azide. Brains were then sectioned in the coronal plane at 30 μ m on a freezing sliding
132 microtome. Each section was collected in 0.01 M phosphate buffered saline (PBS) with 0.02%
133 sodium azide. Alternate serial sections were immunohistochemically stained for primary
134 antibodies listed in Table 1, following the protocol described previously (Wang et al., 2009).
135 Briefly, free-floating sections were incubated with primary antibody solutions diluted in PBS
136 with 0.3% Triton X-100 overnight at 4°C, followed by Alexa-Fluor secondary antibodies (Life
137 Technologies, Carlsbad, CA) either at 1:200 for 4 hours at room temperature or at 1:1000

138 overnight at 4°C. Some sections were counterstained with NeuroTrace (Life Technologies), a
139 fluorescent Nissl stain, at 1:1000 incubated together with secondary antibodies. Sections were
140 then mounted on gelatin-coated slides and coverslipped with Fluoromount-G mounting medium[®]
141 (Southern Biotech, Birmingham, AL).

142 For peroxidase staining with a single antibody, following primary antibody incubation,
143 sections were incubated in a biotinylated IgG antibody (1:200; Vector Laboratories, Burlingame,
144 CA) diluted in PBS with 0.3% Triton X-100 for an hour at room temperature. After washing in
145 PBS, sections were incubated in avidin–biotin–peroxidase complex solution (ABC Elite kit;
146 Vector Laboratories) diluted 1:100 in PBS with 0.3% Triton X-100 for 1 h at room temperature.
147 Sections were then washed in PBS and incubated for 3–5 min in 0.045% 3-3-diaminobenzidine
148 (Sigma, St. Louis, MO, USA) with 0.03% hydrogen peroxide in PB. Sections were mounted on
149 gelatin-coated slides and dehydrated, cleared, and coverslipped with Permount mounting
150 medium (Fisher Scientific).

151 **Quantitative analysis of NM cell body size**

152 This analysis was performed on P12-14 chickens (n=4). For each animal, every fourth sections
153 containing NM were triple labeled for MAP2 and calretinin immunoreactivity as well as for
154 NeuroTrace. This generates 3-4 coronal sections from each animal containing the three NM
155 subregions defined in the current study, NMcm, NMc1, and NMc2 (see Fig. 1 and the Results for
156 the definition of the subregions). All sections were imaged at single focal plane with a 63X
157 objective lens attached to a Zeiss LSM 880 confocal microscope. All images from the same
158 animal were captured using the same imaging parameters. The criteria for including a cell in the
159 subsequent analysis were 1) MAP2 positive, 2) could be unambiguously grouped into either
160 NMcm, NMc1, or NMc2 based on MAP2 and calretinin staining, and 3) having a well-defined

161 cell boundary and an identifiable nucleus in NeuroTrace staining. Cross sectional somatic area of
162 each selected neuron was measured from NeuroTrace staining using Image J (National Institute
163 of Health, USA).

164 To map the somatic area in relationship to the location of each measured neuron, a
165 vertical line was drawn at the location of the most medially located NM neuron measured in one
166 section and served as the Y axis. A horizontal line was drawn at the location of the most
167 ventrally located NM neuron measured in the same section and served as the X axis. The
168 location of each measured neuron was then calculated according to these coordinates using
169 Image J. Somatic areas were presented as the Z axis in relationship to the XY locations as a
170 projection of 3D color map (see Fig. 2E), created using OriginPro (OriginLab, Northampton,
171 MA).

172 For statistical analyses of grouped data across animals, the somatic area of each measured
173 neuron was normalized to the average somatic area of all measured neurons in NMcm of the
174 same animal. The normalized somatic areas of all measured neurons from all three animals were
175 grouped for each NM subregion and compared between NMcm, NMc1, and NMc2. Significance
176 was determined by one-way ANOVA and unpaired t-test using the Prism version 5 software
177 package (GraphPad Software, La Jolla, CA). $P < 0.05$ was considered statistically significant. All
178 data are shown as mean \pm SD in the text and figures.

179 **Cell counting of NM neurons expressing CCK, calretinin or parvalbumin**

180 This analysis was performed on P12-14 chickens for calretinin (n=4) and P6 chickens for CCK
181 (n=3) and parvalbumin (n=3). For each animal, every fourth coronal sections containing the NM
182 were triple labeled for MAP2 immunoreactivity, NeuroTrace, and either CCK, calretinin or
183 parvalbumin immunoreactivity. The caudomost 3 sections contain the main body of NMc1 and

184 NM2c as well as a substantial portion of NMcm and were used for cell counting. MAP2 and
185 NeuroTrace staining were used to identify NM subregions and visualize neuronal cell bodies of
186 all NM neurons. Average optic density of somatic CCK, calretinin or parvalbumin
187 immunoreactivity was measured using Image J. For calretinin and parvalbumin staining, neurons
188 whose staining intensity is 2 standard deviation (SD) above the mean background level were
189 considered as positive neurons. Here the background is referred to a region in the tissue without
190 identifiable cell bodies or processes present. For CCK staining, neurons whose staining intensity
191 is 2 SD above the mean level of NMcm neurons were considered as positive neurons (see Results
192 for the rationale). CCK (or calretinin or parvalbumin) positive neurons were counted in each NM
193 subregions using the cell counter function of Image J. The percentage of CCK (or calretinin or
194 parvalbumin) positive neurons were calculated against the total MAP2-labeled neuronal number.
195 Significance was analyzed by *Chi-square* test using SPSS Statistics package version 19.0 (IBM,
196 Armonk, NY). As a second type of analysis, mean gray scale of CCK immunoreactivity was
197 analyzed by one-way ANOVA and post tested by Bonferroni's Multiple Comparison using
198 Graphpad Prism. $P < 0.05$ was considered statistically significant. All data are shown as mean \pm
199 SD in the text and figures.

200 ***In vitro* single cell filling in brainstem slices**

201 *Slice preparation.* Chicken brainstems at E19 (n=3) were prepared as previously described
202 (Hong et al., 2016). Briefly, the brainstems were dissected out in ice-cold oxygenated ACSF at
203 pH 7.2-7.4, containing the following (in mM): 130 NaCl, 2.5 KCl, 1.25 NaH₂PO₄, 26 NaHCO₃, 1
204 MgCl₂, 3 CaCl₂, and 10 glucose. ACSF was continuously bubbled with a mixture of 95% O₂ /
205 5% CO₂ for dissection and incubation. Coronal sections (300 μ m) containing the caudal NM
206 were prepared with a vibratome (Pelco easiSlicer, Ted Pella, Redding, CA) and collected into a

207 slice incubation chamber. Slices were incubated at 37°C for 40 minutes before switching to room
208 temperature for cell filling.

209 *Cell filling.* Neurons in the caudal NM were individually dye-filled using electroporation
210 (Wang and Rubel, 2012). Briefly, a glass pipette filled with fixable Alexa-Fluor 568 dextran
211 (Invitrogen, Eugene, OR) was driven to approach an identifiable cell body under a Zeiss V16
212 stereo-fluorescence microscope. The dye was introduced into the cell by a positive voltage (15-
213 30V, 20 ms pulse duration, 20 pulses/s, 1-5 s). After electroporation, slices were incubated for
214 another 1-2 minutes to allow dye diffusion to distal dendrites. Slices were then fixed with 4%
215 paraformaldehyde for 15 minutes at room temperature. Following washing with PBS, sections
216 were counterstained with NeuroTrace and mounted on non-coated slides with Fluomount
217 mounting medium. To reduce tissue shrinkage, a nail polish spot was made at each corner of the
218 coverslip to increase the space between the slide and coverslip.

219 *Dendritic structural analyses.* Using the Zeiss LSM 880 confocal microscope, image
220 stacks of each dye-filled neuron were collected with 63x oil-immersion lens at a resolution of
221 0.26 μm per pixel at XY dimensions and with a Z interval of 0.4 μm . These imaging settings
222 provide sufficient resolution for accurate reconstruction and identification of distal ending
223 morphology. Neurons with the entire dendritic arborization contained within one slice were used
224 for subsequent 3D reconstruction. Neurons with dendrites extending outside of the slice were
225 excluded from this analysis. Image stacks were converted into a series of TIFF images in Zeiss
226 Zen Blue software and then imported to NeuroLucida (version 9.03; MBF Bioscience). The entire
227 dendritic arborization was traced with lines through the middle of each branch, as previously
228 described (Wang and Rubel, 2012). Based on this reconstruction, the number of primary
229 dendritic trees and the total dendritic branch length (TDBL) were measured using NeuroLucida

230 Explorer (version 9.03; MBF Bioscience). TDBL was calculated as the sum of the length of all
231 dendritic branches of a neuron. No tissue shrinkage correction was applied.

232 Following imaging, the coverslips were washed with PBS, and the slices were removed
233 from the slides and resectioned at 30 μm . Double immunostaining against MAP2 and calretinin
234 was then performed to determine the location of the filled neurons in NM subregions. TDBL and
235 the number of primary trees were compared between neurons in different NM subregions, using
236 one way ANOVA with unpaired t-test with the Prism. Welch's correction was employed when
237 the variances were not equal. $P < 0.05$ was considered statistically significant. All data are shown
238 as mean \pm SD in the text and figures.

239 ***In vitro* injection into the 8th nerve**

240 E19 chicken embryos (n=6) were used for this experiment. Brainstem blocks of 3-4 mm thick
241 attached with the surrounding skull were prepared in oxygenated ACSF to expose the 8th cranial
242 nerve. The 8th nerve consists of an auditory branch and two vestibular branches (D'Amico-
243 Martel, 1982; D'Amico-Martel and Noden, 1983; Kaiser and Manley, 1996). Prior to injection,
244 the surface of the nerve branches was briefly dried with low-pressure carbogen (95% O₂ / 5%
245 CO₂) blown through a syringe. We then injected the axonal bundle by using a metal needle
246 whose tip was covered with dextran Alexa Fluor 488, 10,000 MW crystals (Molecular Probes,
247 Eugene, OR). For each animal, we made one injection into the auditory branch on one side of the
248 brain and a second injection into the larger bundle of vestibular branches that is located rostral
249 and ventral to the auditory branch on the other side of the brain. After injection, the brainstem
250 chunks were dissected out from the skull with special care to preserve the 8th nerve. The
251 brainstems with attached nerve were then incubated in oxygenated ACSF for another 6 hours at
252 room temperature before immersion fixation with 4% paraformaldehyde overnight at 4°C. After

253 cryoprotection with sucrose, brainstems were sectioned at 30 μm as described above, performed
254 immunostaining or counterstained with NeuroTrace, and mounted on gelatin-coated slides for
255 subsequent imaging.

256 ***In vivo* injection into the superior olivary nucleus (SON)**

257 On the day of hatchling (P0), chickens (n=3) were anesthetized with a ketamine (60 mg / kg) and
258 xylazine (8 mg / kg) cocktail administered intramuscularly. Feathers were plucked from the head
259 and an incision was made to expose the dorsal skull. The animal was secured in a custom
260 stereotaxic head holder designed to allow calibrated rotation of the head. A 0.5 mm hole was
261 drilled 2.0 mm lateral to midline and 0.3 mm caudal to the suture joining the frontal and parietal
262 skull. To target the SON, a glass micropipette (tip diameter 40-60 μm) was filled with 1%
263 cholera toxin B (CTB; List Laboratories, Campbell, CA) and advanced into the brain at a 6-10°
264 rotation in the rostrocaudal axis and a 4° rotation in the mediolateral axis, to a depth of ~9 mm.
265 Tracer was pressure ejected with a Picospritzer II (General Valve Corporation, Fairfield, NJ)
266 using 10-50 ms pulses at 20 psi. The micropipette was retracted, the hole covered with bone wax,
267 and the incision closed. Following survival of 3-6 days, chicks were deeply anesthetized with
268 sodium pentobarbital and transcardially perfused with saline followed by 4% paraformaldehyde.
269 Brains were extracted from the skull and post-fixed for 24 hours in 30% sucrose in
270 paraformaldehyde until sunk. The brains were then sectioned and immunostained for CTB,
271 calretinin, and cholecystokinin (CCK; Table 1). Calretinin and CCK serve as biomarkers for
272 identifying NMc1 and/or NMc2 (see the Result).

273 **Imaging for illustration**

274 Images for illustration were captured either with a Zeiss M2 microscope for bright-field and epi-
275 fluorescent images, or with the Zeiss LSM 880 confocal microscope. Epi-fluorescent images

276 taken with the M2 microscope were treated with the Zeiss Apotome, an optical sectioning
277 approach using structured illumination for reducing out-of-focus information in epi-fluorescent
278 images (Neil et al., 1997; Neil et al., 2000). Photomontages were applied in the Zeiss Zen blue
279 software. Image brightness, gamma, and contrast adjustments were performed in Adobe
280 Photoshop (Adobe Systems, Mountain View, CA). All adjustments were applied equally to all
281 images of the same set of staining from the same animal unless stated otherwise.

282 ***In vitro* electrophysiology in brainstem slices**

283 *Slice preparation.* Acute brainstem slices were prepared from chicken embryos from E20-21, as
284 previously described (Sanchez et al., 2010; Sanchez et al., 2011, 2012b; Sanchez et al., 2015b).
285 Briefly, the brainstem was dissected and isolated in oxygenated low-Ca²⁺ high-Mg²⁺ modified
286 ACSF containing the following (in mM): 130 NaCl, 2.5 KCl, 1.25 NaH₂PO₄, 26 NaHCO₃, 3
287 MgCl₂, 1 CaCl₂, and 10 glucose. ACSF was continuously bubbled throughout the experiments
288 with a mixture of 95% O₂ / 5% CO₂ (pH 7.4, osmolarity 295-310 mOsm/l). The brainstem was
289 blocked coronally, affixed to the stage of a vibratome slicing chamber (Ted Pella, Inc., Redding,
290 CA) and submerged in ACSF. Bilaterally symmetrical coronal slices were made (200 μm thick),
291 and approximately seven slices containing NM were taken from caudal to rostral, roughly
292 representing the low-to-high frequency regions, respectively. The caudomost two to three slices
293 were used in the current study.

294 Slices were collected in a custom holding chamber and allowed to equilibrate for 1 hour
295 at ~22° C in normal ACSF containing the following (in mM): 130 NaCl, 2.5 KCl, 1.25
296 NaH₂PO₄, 26 NaHCO₃, 1 MgCl₂, 3 CaCl₂, and 10 glucose. Normal ACSF was continuously
297 bubbled with a mixture of 95% O₂ / 5% CO₂ (pH 7.4, osmolarity 295-310 mOsm/l). Slices were
298 transferred to a recording chamber mounted on an Olympus BX51W1 (Center Valley, PA)

299 microscope for electrophysiological experiments. The microscope was equipped with a CCD
300 camera, 60x water-immersion objective and infrared differential interference contrast optics. The
301 recording chamber was superfused continuously (Welco, Tokyo, Japan) at room temperature
302 (monitored continuously at $\sim 22^\circ$, Warner Instruments, Hamden, CT) in normal oxygenated
303 ACSF at a rate of 1.5–2 ml/min.

304 *Whole cell electrophysiology.* Current-clamp experiments were performed using an Axon
305 Multiclamp 700B amplifier (Molecular Devices, Silicon Valley, CA). Patch pipettes were pulled
306 to a tip diameter of 1–2 μm using a P-97 flaming/brown micropipette puller (Sutter Instrument,
307 Novato, CA) and had resistances ranging from 3 to 6 $\text{M}\Omega$. The internal solution of patch pipettes
308 was potassium-based and contained the following (in mM): 105 K-gluconate, 35 KCl, 1MgCl₂,
309 10 HEPES-K⁺, 5 EGTA, 4-ATP-Mg²⁺, and 0.3 4-Tris2GTP, pH adjusted to 7.3–7.4 with KOH.
310 The junction potential was ~ -10 mV and was not corrected for current-clamp data reported in this
311 study.

312 After a $\text{G}\Omega$ seal was attained, membrane patches were ruptured and neurons were first
313 held in the voltage clamp mode of whole-cell configuration. A small hyperpolarizing (-1 mV, 30
314 ms) voltage command was presented to monitor whole-cell parameters (i.e., cell membrane
315 capacitance, series resistance and input resistance). NM neurons were included in the data
316 analysis only if they had series resistances < 15 $\text{M}\Omega$. Afterwards we switched to current clamp
317 mode at $I = 0$ for further recordings. Raw data was low-pass filtered at 2 or 5 kHz and digitized
318 at 20 or 50 kHz using a Digidata 1440A (Molecular Devices).

319 Pipettes were visually guided to the caudolateral region of NM, termed NM_c, where
320 neurons were identified and distinguished from surrounding tissue based on cell morphology and
321 location of the nucleus within the slice. In a subset of experiments ($n=7$), 0.1% neurobiotin was

322 added to the pipette solution. Whole-cell patch-clamp recordings were conducted for ~5 min and
323 tissue was immediately fixed in 4% paraformaldehyde. The location and morphology of
324 NMc1/NMc2 neurons were confirmed using confocal microscopy (see Fig. 9A).

325 All experiments were conducted in the presence of a GABA_A-R antagonist picrotoxin
326 (PTX, 100 μM). Synaptic glutamate transmission was continuously blocked using DL-2-amino-
327 5-phosphonopentanoic acid (DL-APV, 100 μM, an NMDA-R receptor antagonist) and 6-Cyano-
328 7-nitroquinoxaline-2, 3-dione (CNQX, 20 μM, an AMPA-R receptor antagonist). Passive
329 membrane properties and action potential (AP) properties were recorded and characterized by
330 using different current clamp protocols. To measure the passive membrane properties, a small
331 hyperpolarizing current was injected into the soma (-10 pA, Franzen et al., 2015, Hong et al.,
332 2016). This paradigm minimizes the recruitment of voltage dependent ion channels that are not
333 active at or near rest. Membrane voltages used for data analysis were averaged over 30 repetitive
334 trials and calculated by fitting a single exponential to the first 30 ms time window following the
335 hyperpolarizing current injection. The membrane input resistance (R_M) was obtained by dividing
336 the calculated steady-state membrane voltage by the injected current. The time constant of the
337 membrane voltage (τ_M) was quantified by fitting a single exponential as described above and
338 membrane capacitance (C_M) was calculated as $C_M = \tau_M / R_M$. Action potential (AP) threshold
339 current is defined as the minimum amount of current required for neurons to generate an AP
340 ~50% of the time across 30 repetitive stimulations (interpulse stimulus intervals = 2 s). Once AP
341 threshold current was obtained, a sustained current command (duration = 100 ms) was injected
342 into the soma at 25% above the measured threshold current for each neuron. APs evoked by this
343 current command were used to characterize AP properties. Each AP property was measured and
344 averaged over 30 repetitive trials.

345 *Data analysis.* Recording protocols were written and run using Clampex acquisition and
346 Clampfit analysis software (version 10.3; Molecular Devices, Silicon Valley, CA). Statistical
347 analyses and graphing protocols were performed using Prism (GraphPad versions 6.07) and
348 MATLAB (version R2014b; The Math Works, Natick, MA) software. Correlation analyses were
349 conducted to explore the relationships between AP properties and reported as Pearson product-
350 moment correlation (r). A linear regression was fitted to scatter plots. The standard for a
351 significant correlation was defined as $p < 0.05$. All data are shown as mean \pm 1 SD in the table
352 and text.

353 *Reagents.* All bath applied drugs were allowed to perfuse through the recording chamber
354 for ~10 minutes before subsequent recordings. DL-APV, CNQX and all other salts and
355 chemicals were obtained from Sigma-Aldrich (St. Louis, MO). PTX were obtained from Tocris
356 (Ellisville, MO). Neurobiotin was obtained from Vector Laboratories (Burlingame, CA).

357

358 **Results**

359 **The caudal NM contains two neuronal groups with dendrites, NMc1 and NMc2.**

360 The classical NM neurons are characterized by a round, bald soma with no or only 1-2 short
361 dendrites (Cajal, 1909; Jhaveri and Morest, 1982). This adendritic morphology, however, is not
362 common to neurons in the caudal NM. To visualize neuronal dendrites, we first examined the
363 distribution pattern of MAP2 immunoreactivity, which labels all neuronal somata and dendrites
364 (Fig. 1). As expected, the middle and rostral portions of NM display strong somatic staining
365 without substantial dendritic structure (Fig. 1C-D). At the caudal level, this staining pattern is
366 restricted to the medial region, referred to as the caudomedial NM (NMcm) for subsequent
367 description (Fig. 1B). In contrast, extensive dendritic staining is seen in the lateral region of the

368 caudal NM (Fig. 1B) as well as the most caudal pole of the NM (Fig. 1A). High-magnification
369 observations further revealed that the caudolateral NM containing neuronal dendrites is divided
370 into two subregions, here named NMc1 and NMc2 (Fig. 1E-H). NMc1 is located immediately
371 adjacent to adendritic neurons in NMcm. NMc2 surrounds NMc1 caudally and laterally, and
372 occupies the most caudal pole of NM. As compared to NMc1, NMc2 shows longer MAP2-
373 stained dendritic branches and overall higher intensity of MAP2 immunostaining. We further
374 mapped the relative location of NMc1 and NMc2 along the caudal-rostral axis in series coronal
375 sections through NM (Fig. 1I). NMc1 and NMc2 are found in the most caudal one third of the
376 entire NM. NMc1 and NMcm usually disappear from the most caudal coronal section,
377 approximately corresponding to only 2% of the caudal-rostral axis.

378 MAP2-stained neuronal cell bodies in NMc1 and NMc2 appear smaller in size than those
379 in NMcm (Fig. 1G). To quantitatively confirm this observation, we measured cross-sectional
380 somatic area of NM neurons from sections stained with NeuroTrace, a fluorescent Nissl stain,
381 and MAP2 (Fig. 2A-C). We first mapped the somatic area to the location of measured cells in
382 individual coronal sections as a projection of 3D heat map (Fig. 2D-E). This map clearly shows
383 larger cell body sizes in NMcm (warm colors in Fig. 2E) and smaller cell body sizes in NMc1
384 and NMc2 (cold colors). This general distribution pattern is found in all animals examined.
385 Notably, although cells of different sizes are intermingled in both NMc1 and NMc2, the majority
386 of cells with the smallest cell body sizes (blue color) are located in NMc2. Interestingly, NMc2
387 also contains a small number of neurons with relatively large cell body sizes as shown in warm
388 colors. These large cells are found widely in NMc2, although they tend to cluster in the most
389 lateral region of NMc2 in some animals (arrow in Fig. 2E). Statistical analysis on population
390 data across sections and animals further confirmed that the somatic area in NMcm ($n = 63$ cells

391 from 3 animals) is significantly larger than that in NMc1 ($n = 62$ cells from 3 animals, $p <$
392 0.0001) and NMc2 ($n = 63$ cells from 3 animals, $p < 0.0001$; Fig. 2F). In addition, the somatic
393 area of the neurons in NMc1 is significantly larger than that in NMc2 ($p < 0.0001$).

394 To further examine the dendritic morphology of individual neurons in NMc1 and NMc2,
395 we filled individual cells with a fluorescent dye in the caudal NM. Figure 3A shows a coronal
396 brainstem slice containing NMcm, NMc1 and NMc2 located from medial to lateral. Consistent
397 with the observations from MAP2 staining, filled neurons in the most medial NM have either no
398 dendrites or only one short dendrite (Fig. 3D, H), while neurons located more laterally show
399 extensive dendrites. In particular, filled neurons in the most lateral portion where NMc2 is
400 located show notably more dendritic branches (Fig. 3B, E, F) than the neurons in NMc1 (Fig.
401 3C, G). We further quantified dendritic structural properties based on 3D reconstruction of the
402 dendritic arborization of individual filled neurons. As expected, the total dendritic branch length
403 (TDBL) of NMcm neurons ($18 \pm 17 \mu\text{m}$; $n = 6$ cells from 3 animals) is significantly smaller than
404 that of NMc1 ($392 \pm 204 \mu\text{m}$; $n = 5$ cells from 3 animals; $p = 0.0148$) and NMc2 neurons (1577
405 $\pm 294 \mu\text{m}$; $n = 6$ cells from 3 animals; $p < 0.0001$; Fig. 3I). In addition, the TDBL of NMc2
406 neurons is significantly larger than that of NMc1 neurons ($p < 0.0001$). Similarly, NMcm
407 neurons have less than two primary dendrites on average (1.2 ± 0.8), significantly less than
408 NMc2 (25.3 ± 6.5 ; $p = 0.0003$) and NMc1 neurons (14.2 ± 4.8 ; $p = 0.0039$; Fig. 3J). NMc2
409 neurons have significantly more primary dendrites than NMc1 neurons ($p = 0.011$). Importantly,
410 increases in TDBL from NMcm to NMc1 and from NMc1 to NMc2 are rather robust; there is no
411 overlap of the TDBL ranges between the three regions. Together, these data demonstrate
412 significantly increasing dendritic size and complexity from NMcm to NMc1 and from NMc1 to
413 NMc2.

414

415 **NMc2 is distinct from other NM portions in CCK distribution.**

416 Cholecystokinin (CCK) is a broadly expressed peptide hormone in mammalian and avian brains,
417 known as a biomarker for specialized auditory neurons with distinct physiological properties (Li
418 et al., 2014). Double immunostaining of MAP2 and CCK in the NM demonstrates that CCK
419 immunoreactivity is prominent in NMc2 and was detected in both cell bodies and the most
420 proximate portion of dendrites (Fig. 4). CCK immunoreactivity was also detected in the neuropil
421 regions that are overlapped with MAP2 staining. Although most MAP2-immunoreactive neurons
422 in NMc2 are strongly labeled for CCK (arrows in Fig. 4D), some neurons display only
423 background levels of CCK signal (arrowheads in Fig. 4D). Occasionally, a few neurons with
424 strong CCK labeling were found in NMc1 (arrows in Fig. 4B2). In contrast, all neurons in
425 NMcm or more rostral portions of NM as well as the majority of the neurons in NMc1 display a
426 low level of staining slightly above the background (Fig. 4B-C). Statistical analysis confirmed
427 that NMc2 neuronal cell bodies show significantly stronger CCK immunoreactivity (67.5 ± 32.7 ;
428 $n = 109$ cells from 3 animals) than those of NMcm (38.0 ± 12.8 ; $n = 151$ cells from 3 animals, p
429 <0.0001) and NMc1 (47.7 ± 14.4 ; $n = 96$ cells from 3 animals, $p <0.0001$; Fig 4E). Using 2 SD
430 above the average somatic CCK immunostaining intensity across all measured NMcm neurons as
431 cutoff, the percentage of CCK positive neurons in NMc2 ($70.8 \pm 18.4\%$) is significantly larger
432 than that in NMcm ($2.3 \pm 2.8\%$; $n = 151$ cells from 3 animals, $p = 0.0012$) and NMc1 ($24.8 \pm$
433 24.5% , $p = 0.0156$; Fig. 4F). The difference between NMcm and NMc1 is not significant ($p =$
434 0.3213), due to the high heterogeneity of NMc1 neurons in CCK expression. These results
435 indicate that NMc2 is distinct from other NM regions in the distribution of CCK.

436

437 **NMc1 and NMc2 receive inputs from the auditory nerve.**

438 The caudolateral NM was initially considered as a vestibular group in pigeons (Boord and
439 Rasmussen, 1963), and later is reported to be auditory in chickens (Kaiser and Manley, 1996)
440 and barn owls (Köppl and Carr, 1997). To further clarify the nature of NMc1 and NMc2
441 identified here, we mapped terminal distribution patterns of auditory and vestibular axons of the
442 8th nerve in brainstem chunk preparations. Since both the auditory and vestibular nerves project
443 exclusively ipsilaterally to the dorsal brainstem (Parks and Rubel, 1978; Kaiser and Manley,
444 1996), we injected a fluorescent dextran dye in the auditory nerve branch on one side of the brain
445 and made a second injection into the large vestibular nerve branch on the other side of the brain
446 of the same chunk preparations for comparison (Fig. 5A).

447 On the side with injections into the auditory nerve branch (Fig. 5B), we found labeled
448 axons and terminals throughout NM including NMc1 and NMc2 (Fig. 5C-E). As expected,
449 labeled terminals form large end-bulb synapses surrounding the neuronal cell bodies in NMcm
450 and the more rostral portion of NM (Fig. 5C, F). In contrast, NMc1 and NMc2 contain only
451 bouton-like terminals, which are often found in the space between cell bodies, presumably on
452 dendrites (Fig. 5D, G, H). Double labeling with the synaptosomal-associated protein 25
453 (SNAP25), a presynaptic marker for excitatory synapses (Oyler et al., 1989; Safieddine and
454 Wenthold, 1999), confirmed that bouton-like terminals in NMc1 and NMc2 are excitatory,
455 similar to end-bulbs in NMcm (Fig. 5I). As expected, NMcm displays characterized perisomatic
456 staining pattern of SNAP25 (Fig. 5J) and intensive neuropil staining in NMc1 and NMc2 (Fig.
457 5K-L). No labeled terminals were found in the adjacent vestibular nuclei (Fig. 5M). These results
458 demonstrate that NMc1 and NMc2 receive excitatory inputs from the auditory nerves through
459 bouton-like terminals.

460 On the side with injections into the vestibular branch (Fig. 5N), no labeled axons and
461 terminals were found in NM (Fig. 5O) and other auditory cell groups in the brainstem including
462 nucleus angularis (NA) and nucleus laminaris (NL). Whereas, we did find labeled terminals in
463 vestibular regions located adjacent to NA and NM (Fig. 5P). It is important to note that this
464 observation does not exclude the possibility that NMc1 and NMc2 receive inputs from other
465 vestibular nerve and nuclei.

466

467 **NMc1 and NMc2 receive inhibitory inputs from the superior olivary nucleus (SON).**

468 Inhibition is an essential mechanism for precise temporal processing in NM (Burger et al., 2011).
469 To investigate the inhibitory input to the caudal NM, we first examined the distribution pattern of
470 gephyrin, a postsynaptic protein that anchors inhibitory neurotransmitter receptors to the
471 cytoskeleton (Kirsch et al., 1993; Lim et al., 2000). Consistent with previous studies using
472 GABA receptors as an inhibitory synaptic marker (Burger et al., 2005b), gephyrin
473 immunoreactivity forms a perisomatic staining pattern in NMcm (Fig. 6A-B). This staining
474 pattern is absent in NMc1 and NMc2 (Fig. 6C-D). Instead, gephyrin immunoreactivity is
475 scattered between the cell bodies in these two regions.

476 To further identify the source of inhibition in NMc1 and NMc2, we injected cholera toxin
477 B (CTB), a sensitive neural tract tracer, into the superior olivary nucleus (SON) *in vivo*. SON
478 receives excitatory input from NA and NL and is the major source of inhibition to NA, NM, and
479 NL (Burger et al., 2005a). Figure 6 demonstrates a case with CTB injection into a large portion
480 of SON and the surrounding area (Fig. 6M). As expected, no labeled cell bodies were detected in
481 NM, while labeled terminals were found throughout NM including NMcm, NMc1, and NMc2
482 (Fig. 6E-H, J). Similar to the staining pattern of gephyrin immunoreactivity, CTB labeled

483 terminals often surround the cell bodies in NMcm and the higher frequency region of NM, while
484 displaying a diffused pattern in NMc1 and NMc2. On the contrary, both labeled neuropils and
485 cell bodies were found in NA and NL (Fig. 6K-L).

486

487 **NMc1 and NMc2 show differential expression patterns of calcium binding proteins.**

488 Expression of various calcium binding proteins in auditory neurons displays cell-type specificity
489 and species variation (Takahashi et al., 1987; Rogers, 1989; Li et al., 2013). In chickens, it is
490 reported that all neurons in NM express calretinin but not parvalbumin, two EF-hand calcium
491 binding proteins (Rogers, 1987, 1989). Here we examined the localization of these two proteins
492 in NMc1 and NMc2.

493 Double labeling of calretinin and MAP2 reveals a highly differential distribution pattern
494 of calretinin in the three NM subregions identified based on the basis of MAP2 staining pattern
495 (Fig. 7A). As expected, most neurons in NMcm (~91%) and the more rostral portion of NM
496 display strong somatic staining of calretinin in the cytoplasm, although the staining intensity
497 varies across neurons (Fig. 7B, E). In many neurons, significant staining in the nucleus is also
498 present and often more intense than the cytoplasmic staining (arrows in Fig. 7B2). About 66% of
499 neuronal cell bodies in NMc1 are calretinin immunoreactive, although the staining intensity is
500 generally lower than the neurons in the adjacent NMcm (Fig. 7C, E). In NMc1, calretinin
501 staining intensities in the nucleus and cytoplasm are largely comparable. Calretinin labeled
502 dendrites are also seen in this region. In contrast, calretinin immunoreactivity is strikingly low in
503 NMc2 (Fig. 7D2). Only 8% of neuronal cell bodies in NMc2 display weak calretinin
504 immunostaining above the background level and these neurons are often located close to NMc1
505 (dashed lines and inset in Fig. 7D2, E). A sharp border between NMc1 and NMc2 is clear based

506 on calretinin immunostaining. Statistical analysis further verified the differential expression
507 pattern of calretinin along the tonotopic axis. The percentage of calretinin positive neurons in
508 NMcm ($91 \pm 5\%$; $n = 426$ cells from 3 animals) is significantly larger than that in NMc1 ($66 \pm$
509 11% ; $n = 397$ cells from 3 animals, $p < 0.001$) and NMc2 ($8 \pm 3\%$; $n = 474$ cells from 3 animals,
510 $p < 0.001$). In addition, the percentage of calretinin positive neurons in NMc1 is also
511 significantly larger than that in NMc2 ($p < 0.001$; Fig. 7E).

512 Double labeling of MAP2 and parvalbumin (Fig. 8) provided a strikingly different
513 pattern. Low-magnification images show strong parvalbumin immunoreactivity throughout NM
514 (Fig. 8A). Closer views of NMcm and the more rostral NM reveal intense neuropil staining
515 surrounding unstained NM cell bodies (arrowheads in Fig. 8B). These parvalbumin labeled
516 processes resemble the end-bulbs of the auditory nerve in morphology and location. Neuropil
517 staining is also abundant in NMc1 and NMc2, primarily present as neuronal processes of small
518 calibers. A small population of MAP2-labeled cell bodies were double labeled for parvalbumin
519 (arrows in Fig. 8B-E). They were encountered more frequently in NMc1 than in NMcm and
520 NMc2. Statistical analysis on population data across sections and animals further confirmed that
521 the percentage of parvalbumin positive neurons in NMc1 ($10.3 \pm 1.6\%$; $n = 275$ cells from 3
522 animals) is significantly larger than that in NMcm ($4.9 \pm 3.0\%$; $n = 473$ cells from 3 animals, $p <$
523 0.001) and NMc2 ($3.0 \pm 0.9\%$; $n = 297$ cells from 3 animals, $p < 0.001$). In addition, the
524 percentage of parvalbumin positive neurons in NMcm is comparable to that in NMc2 ($p = 0.569$;
525 Fig. 7E). Together, NMc1 contains neurons expressing calretinin and parvalbumin, whereas most
526 neurons in NMc2 do not express these two proteins at a detectable level.

527

528 **NMc1 and NMc2 neurons show distinct passive and active membrane properties**

529 We explored passive and active membrane properties of NMc1/NMc2 neurons and when
530 appropriate, compared them with mid- to high-frequency NM neurons. Neuronal location and
531 morphology were confirmed using neurobiotin for a subset of experiments. An example of a
532 neurobiotin-labeled neuron is shown in Fig. 9A. This neuron was located within the region of
533 NMc1 and NMc2; lateral to NMcm (inset) and contained multiple dendritic processes. Despite
534 the clear anatomical distinctions noted above, from an electrophysiological perspective we were
535 not able to differentiate NMc1 and NMc2 neurons. Instead, we used membrane capacitance as an
536 index for neuron size (i.e., surface area) with the idea that NMc2 neurons would present with a
537 larger membrane capacitance than NMc1 neurons. An example of the recording protocol and
538 membrane response is shown in Fig. 9B (see Methods for calculation of membrane capacitance).
539 We found the following evidence that supports the use of membrane capacitance as an indicator
540 of neuronal size. First, individual brainstem slices were placed in a custom chamber that
541 maintained the tonotopic gradient, from the caudmost slice to the rostromost slice representing
542 slices one to seven respectively. As mentioned in the Methods section, the caudmost two to
543 three slices were used for NMc recordings. According to our anatomical data (see Fig. 1A, E),
544 NMcm neurons are not observed in the caudmost slice. The majority of neurons in the
545 caudmost slice are NMc2 neurons and indeed present with a larger estimated membrane
546 capacitance (Fig. 9C, caud-mos slice). Also, when compared to mid- to high frequency NM
547 neurons (e.g., neurons taken from slices shown in Fig. 1C-D, Fig. 9C, mid-ros slices, Hong et al.,
548 2016), NMc2 neurons have significantly larger membrane capacitance (42.83 ± 10.50 pF *versus*
549 26.15 ± 4.60 pF). The difference in membrane capacitance is likely due to extensive dendrites
550 (despite smaller soma) of NMc2 neurons compared to adendritic NM neuron (despite larger
551 soma).

552 Second, when NMcm neurons begin to gradually appear, the second and third slice
553 contains both NMc1 and NMc2 neurons (see Fig. 1B, F, G). Post-hoc test of membrane
554 capacitance did not result in significant difference between neurons taken from the second and
555 third caudal slices (Fig. 9C, caud slices) compared to neurons taken from the caudomost slice,
556 albeit NMc2 neurons presented with a larger membrane capacitance on average. The lack of
557 significance is likely due to the intermingled distribution pattern of NMc1 and NMc2 in the
558 caudal slices. Additionally, membrane capacitance of second and third caudal slices is not
559 significantly different from that of higher frequency NM (Fig. 9C, mid-rostral slices), likely due
560 to the fact that membrane capacitance of mid- to high frequency NM neurons is relatively
561 homogeneous, i.e., the capacitance values for individual neurons vary minimally from the
562 average (26.15 ± 4.6 pF, Hong et al., 2016). This result is in line with homogeneity of NM
563 neuronal size. In contrast, we observed a large variability for NMc neurons. In particular, five
564 NMc neurons obtained from the second caudal slice presented with smaller capacitance than the
565 average of mid- to high frequency NM neurons. Their smaller membrane capacitance is
566 reminiscent of properties of NMc1 neurons located adjacent to the NMcm region, which show
567 significantly smaller somatic area and minor dendritic processes (see Fig. 2, 3C, G). As a result,
568 these NMc1 neurons showed even smaller capacitance than traditional NM neurons and thus led
569 to the non-significance reported in Fig. 9C. Taken together, membrane capacitance is a relatively
570 reliable measurement of neuronal size for NMc neurons. NMc1 neurons present with smaller
571 membrane capacitance. This is likely due to their smaller soma and less complex dendritic
572 arborization (as compared to NMc2, see Fig. 3), while NMc2 neurons usually present with larger
573 membrane capacitance due to their more extensive dendritic processes.

574 We compared membrane capacitance among NMc1/NMc2 neurons and examined

575 whether neurons with larger membrane capacitance (i.e., likely NMc2 neurons) show distinct
576 intrinsic properties compared to neurons with smaller membrane capacitance (i.e., likely NMc1
577 neurons); serving as an indirect method to classify NMc1 and NMc2 AP properties. It should be
578 noted that comparisons of all passive membrane properties (i.e., resting membrane potential,
579 time constant, input resistance and membrane capacitance) were made under the same
580 experimental conditions (e.g., room temperature) and were significantly different from higher
581 frequency NM neurons (Table 2).

582 AP properties of interest are highlighted in Fig. 9D from a representative E21 neuron. In
583 order to compare AP properties across different NM regions, APs were evoked using a sustained
584 current injection (100 ms) set at 25% above threshold current. Three variables were analyzed
585 regarding AP kinetics: maximal rise rate, fall rate and half width. Rise and fall rates were
586 calculated as the maximum rate of increase and decay in the AP depolarizing and repolarizing
587 phase, respectively. Half width was quantified as AP duration measured at half of the maximum
588 amplitude relative to the resting membrane potential. To quantify AP reliability, we stimulated
589 neurons using sustained suprathreshold current depolarization (i.e., 25% above threshold current)
590 across 30 trials (interpulse stimulus intervals = 2 s) and calculated the range of time points of AP
591 peak occurrence.

592

593 **NMc1 and NMc2 neurons show distinct and heterogeneous AP properties.**

594 A biophysical hallmark of mid- to high-frequency NM neurons is the generation of a single onset
595 AP in response to sustained depolarization (Reyes et al., 1994; Howard et al., 2007; Hong et al.,
596 2016). We found several AP properties of NMc1 and NMc2 neurons that were notably different
597 from this biophysical phenotype of NM neurons. These include increased excitability and slower,

598 less reliable APs (Table 2). In the following sections, we report these differences in greater
599 detail.

600 Fig. 10 A-C shows representative recording from three different NMc1/NMc2 neurons.
601 Using current commands ranging from -100 pA to +80 pA, NMc1/NMc2 neurons fired a range
602 of APs to sustained suprathreshold depolarization, from multiple spikes to a single spike (Fig. 10
603 A-C, *top*, respectively). Threshold current required to elicit an AP was approximately an order of
604 magnitude lower for NMc1/NMc2 compared to higher frequency NM (Table 2). For all three
605 NMc1/NMc2 neurons shown in Fig. 10, the threshold current was < 110 pA with the lowest
606 current being 20 pA (Fig. 10A). NMc1/NMc2 neurons presented with a range of excitability
607 when a suprathreshold current command 25% above threshold current was applied. For the
608 neuron shown in Fig. 10A, a weak depolarizing current injection of 23 pA resulted in sustained
609 AP firing with highly variable first spike occurrence and considerable spontaneous activity long
610 after the completion of the sustained current (Fig. 10A, *middle*, arrowhead and arrow,
611 respectively). With a suprathreshold current injection of 200 pA, the neuron responded with
612 multiple spikes that continuously declined in AP amplitude during the duration of the stimuli
613 (Fig. 10A, *bottom*). The AP amplitudes halfway through the sustained current injection (i.e., 50
614 ms after the stimulus onset) were reduced by 36% on average (n=6) and these neurons presented
615 with depolarization block at the end of the injected current time window.

616 These results were partially true for the neuron shown in Fig. 10B. When sustained
617 current injections ranging from -100 pA to +80 pA were applied, strengths greater than 60 pA
618 resulted in multiple spiking (Fig. 10B, *top*) but a current injection 25% above threshold (i.e., 44
619 pA) resulted in a single onset AP (Fig. 10B, *middle*). The time of the “single-spike” peak
620 occurrence across 30 trials was highly variable (i.e., large AP reliability range, inset). For the

621 population of neurons that presented with this response property (n=11), AP reliability range was
622 significantly larger compared to mid- to high-frequency NM neurons (5.28 ± 4.41 ms, $p <$
623 0.0001 , Table 2). In addition, this neuron fired tonically throughout the duration of the
624 suprathreshold current injection (i.e., 200 pA) with no rundown of AP amplitudes (Fig. 10B,
625 *bottom*).

626 The single AP phenotype that is typical of mid- to high-frequency NM was also
627 occasionally observed. For the neuron shown in Fig. 10C, current injections ranging from -100 to
628 +125 pA resulted in a single AP (*top* and *middle*, respectively) but the time of peak AP
629 occurrence was somewhat variable (inset) and not as reliable as compared to higher frequency
630 NM neurons (4.48 ± 4.72 ms, $p < 0.0001$, Table 2). Interestingly, when we systematically
631 increased the strength of current injections beyond the 25% criteria, all of these “single spiking”
632 neurons generated multiple APs (Fig. 10C, *bottom*, Fig. 10D). Only one quarter of recorded
633 neurons (6 out of 23) resulted in this response property, suggesting that a subpopulation of
634 NMc1/NMc2 neurons resembles some aspects of mid- to high-frequency NM neurons, albeit
635 minimally.

636 Regardless of the heterogeneity of active membrane properties, all NMc1/NMc2 neurons
637 increased their AP output as a function of the increasing strength of current injection, which is
638 markedly distinct from traditional NM (Fig. 10D). As such, we used the neuron’s input/output
639 function to objectively categorize a neuron’s firing pattern into three types. The “A-like” neurons
640 (reference to Fig. 10A) and the “B-like” neurons (reference to Fig. 10B) both generated multiple
641 APs at the moderate current levels of ~80 pA. When increasing the current strength, the “A-like”
642 neurons responded in a nonmonotonic fashion that resulted in reduced spike output at higher
643 current strengths (e.g., 200 pA, Fig. 10D). In contrast, the “B-like” neurons fired multiple APs (>

644 6) in a monotonic fashion with increasing current strength (Fig. 10D). Finally, the “C-like”
645 neurons (reference to Fig. 10C) generated a single AP to moderate current injections but fired
646 several APs (< 4) in a monotonic fashion to increasing current strength (Fig. 10D). It should be
647 noted that the firing of multiple APs during sustained depolarization is not observed in late-
648 developing neurons of surrounding temporal coding brainstem nuclei (e.g., NL and more
649 rostromedial NM) regardless of the strength and duration of current injection (Fig. 10D, Hong et
650 al., 2016).

651 It should also be noted that the different spiking activity was not due to differences in
652 neuronal integrity of NMc1/NMc2 neurons. Across the three NMc groups, we found no
653 significant differences in resting membrane potential (RMP, Fig. 10E, $p = 0.21$) and input
654 resistance (Fig. 10F, $p = 0.25$), both of which are indicators of neuronal integrity. Despite the
655 relative homogeneity of NMc neuronal integrity, “C-like” neurons did show a more
656 hyperpolarized RMP and lower input resistance, suggesting their underlying ion channel
657 conductances might differ from other NMc neurons.

658 Based on these observations, we speculate that there is a population gradient of active
659 membrane properties that results in diverse firing patterns among NMc1/NMc2 neurons. This
660 speculation is supported by the significant correlation between the number of APs generated and
661 threshold current (Fig. 11A), along with the significant correlation between threshold current and
662 input resistance (Fig. 11C). These results indicate that NMc1/NMc2 neurons with lower
663 threshold currents can fire multiple APs to sustained depolarization (i.e., more excitable than
664 those with higher threshold currents), and have a higher input resistance. This is consistent with
665 the expression gradient of $K_{v1.1}$, the alpha subunit associated with the low-voltage activated
666 potassium channel responsible for single-spiking behavior (Fukui and Ohmori, 2004). Because

667 the low-voltage activated potassium channels generate an outward current partially activated at
668 rest (Rathouz and Trussell 1998; Howard and Rubel 2010), one would expect that less excitable
669 neurons also exhibit lower input resistance than those with higher excitability. Indeed, the “C-
670 like” NMc neurons have a lower input resistance and more hyperpolarized RMP than the “A-
671 like” and “B-like” neurons (Fig. 10E-F). This is further supported by the significant correlation
672 between threshold current and membrane capacitance (Fig. 11B), indicating that NMc2 neurons
673 have larger surface area and are more excitable than NMc1. Not surprisingly, we found a
674 significant correlation between membrane capacitance and input resistance ($r = 0.66$, $p < 0.01$,
675 data not shown). Therefore, we used threshold current, membrane capacitance and input
676 resistance as indices of excitability for individual NMc1/NMc2 neurons, and explored whether
677 this gradient of excitability affects AP properties using correlation analyses.

678 We did not find a significant correlation with AP rise rate for either threshold current,
679 membrane capacitance or input resistance (Fig. 11D), indicating that rise rate is less prone to
680 population gradient of excitability. This is further supported by the non-significant difference in
681 rise rate between NMc1/NMc2 and higher frequency NM neurons (Table 2). In contrast, AP fall
682 rate was significantly correlated with threshold current, membrane capacitance and input
683 resistance (Fig. 11E). Neurons with larger capacitance, lower thresholds and higher input
684 resistance (i.e., NMc2 neurons) are more likely to have slower repolarization. As a result, AP
685 half width was also significantly correlated with all three variables (Fig. 11F), indicating that
686 larger, more excitable and less permeable neurons (i.e., NMc2 neurons) have wider APs. Finally,
687 AP reliability range was also significantly correlated with threshold current, membrane
688 capacitance and input resistance (Fig. 11G), indicating that leakier neurons with less surface area
689 and higher threshold currents (i.e., NMc1 neurons) generate more temporally reliable APs.

690 To summarize, we observed clear heterogeneity of evoked activity for NMc1/NMc2
691 neurons. Ongoing experiments are determining the underlying synaptic and intrinsic mechanisms
692 and whether this heterogeneity is associated with anatomically and biochemically distinct
693 neuronal types.

694

695 **Discussion**

696 The current study characterizes multiple neuron types in the caudolateral region of the avian
697 cochlear nucleus, nucleus magnocellularis (NMc1 and NMc2). These neuron types display
698 unique cellular morphology, molecular signatures and biophysics, distinct from traditional
699 definitions of NM neurons (Fig. 12). Below we compare the structural and functional properties
700 of NMc1 and NMc2 neurons with previous studies in the caudolateral NM and discuss potential
701 mechanisms underlying these unique properties.

702 **Definition of NMc**

703 The chicken NMc, as identified in this study, is the most caudolateral portion of NM where
704 neurons possess extensive dendrites and synapses with small bouton-like axonal terminals from
705 the auditory nerve. In contrast, well-characterized neurons located in the major body of NM
706 which is rostromedial to NMc, lack substantial dendritic structure and are innervated by large
707 somatic synapses (i.e., the End Bulbs of Held) from the auditory nerve.

708 NMc represents the low frequency range of the avian tonotopic axis. According to the
709 tonotopic organization of the chicken NM (Rubel and Parks, 1975), NM neurons with
710 characteristic frequency (CF) from 170 to 4100 Hz are located progressively from caudolateral to
711 rostromedial. Due to the technical limitation of this aforementioned study, which did not
712 generate acoustic stimuli below 100 Hz, CF ranges in a most caudolateral region was not

713 determined, giving rise to the initial notion that this NM regions is non-auditory. Subsequent
714 studies did record NM neurons approximately in the caudal region that respond to tones as low
715 as 10 Hz in frequency, although their exact location was not specifically mapped in relationship
716 to the tonotopic organization (Warchol and Dallos, 1990). Consistently, behavioral studies
717 confirmed that chickens hear as low as 2 Hz (Hill et al., 2014). Combined tract tracing and
718 physiological studies further demonstrated that the NM region containing bouton terminals
719 corresponds to frequencies < 500 Hz of the tonotopic map (Fukui and Ohmori, 2004). Taken
720 together, we propose that NMc in chickens contains CFs below 500 Hz and is divided into NMc1
721 and NMc2. NMc1 corresponds to the low frequency NM defined by Fukui and Ohmori (2004)
722 with approximate CFs of 100-500 Hz, while NMc2 region coincides with even lower CFs below
723 100 Hz that was previously considered *non-auditory* in chickens by Rubel and Parks (1975) as
724 well as in pigeons (Boord and Rasmussen, 1963). Further *in vivo* recordings are needed to map
725 the precision of the tonotopic organization in these two regions and the exact location of NM
726 neurons with CFs below 100 Hz.

727 An important question is whether there is a clear boundary between NMc1, NMc2 and
728 the remaining NM. NM is known to have gradients in cellular morphology and physiology along
729 their tonotopic axis (Rubel and Fritzsche, 2002). Indeed, when looking at single metric (dendritic
730 arborization, synaptic terminal morphology, or physiological response), the caudal NM gradually
731 increases the magnitude of its divergence from the relatively homogeneous morphology and
732 physiology observed in more rostral NM. We suggest, however, that the distinct morphological
733 and physiological features of the regions we have called NMc1 and NMc2 produce break points
734 in the continuum to form distinct groups of cells which could possibly have distinct functions or
735 adopt distinct mechanisms for accomplishing similar functions. Although the borders are blurry

736 with a number of single metric, the break points are clear when considering the composite
737 anatomical and physiological profiles of the neurons, particularly when combined with the fairly
738 discrete variations in protein expression. This proposal is also supported by studies in barn owls,
739 another avian species in which the low frequency NM has been studied (Takahashi and Konishi,
740 1988; Köppl, 1994; Köppl and Carr, 1997). The barn owl low frequency NM, as similarly
741 defined as a caudolateral region containing long dendrites and bouton-like synapses, displays
742 two unique cell types with distinct dendritic morphology, consistent with the heterogeneity of the
743 chicken NMc.

744 **Differential expression of calcium binding proteins in NM**

745 In addition to structural specializations, our data further revealed that NMc1 and NMc2 neurons
746 express a unique set of calcium binding proteins and neuropeptides. Previous studies reported
747 that the chicken NM neurons express calretinin but not parvalbumin (Rogers, 1989; Parks et al.,
748 1997; Stack and Code, 2000). Our data confirmed this expression pattern in the adendritic
749 portion of NM, but we found that most neurons in NMc2 do not express calretinin. This
750 difference is likely due to possible overlook of this caudal cell group with negative calretinin
751 staining in previous studies. Lack of calretinin expression in NMc2 is consistent with calretinin-
752 negative neurons in the ventral nucleus angularis (NA, low frequency) (Bloom et al., 2014),
753 indicating this maybe a common feature for the low frequency neurons in the chicken cochlear
754 nuclei. In addition, we found parvalbumin expressing neurons in NM including NMc1 and
755 NMc2. Similarly, the majority, if not all, of NM neurons co-express these two calcium binding
756 proteins in the zebra finch (Li et al., 2013), emu (MacLeod et al., 2006) and owl (Takahashi et
757 al., 1987; Kubke et al., 1999). Calretinin and parvalbumin have fast and slow calcium binding
758 kinetics, respectively, which are fine-tuned by instantaneous intracellular calcium concentration.

759 They can work together to modulate global and local intracellular calcium signals in the same
760 cell (Dargan et al., 2004). Differential expression of various calcium binding proteins has been
761 associated with cell type specific calcium regulation and cellular physiology (Nejatbakhsh and
762 Feng, 2011). In this study, we observed that the percentage of calretinin or parvalbumin
763 expressing neurons are comparable between NMcl and NMcm, suggesting that the chicken
764 NMcl may share some common mechanisms with NM neurons in calcium regulation. On the
765 other hand, these calcium binding proteins may not be critical for NMc2 neurons.

766 It is important to point out that calretinin plays an important role in modulating neuronal
767 excitability. In calretinin-knockout mice, GABAergic interneurons in the hippocampus express
768 excess GABA, which leads to impaired long-term potentiation induction of dentate gyrus cells
769 (Schurmans et al., 1997). Similarly, cerebellar granule cells lacking calretinin show increased
770 excitability, indicated by faster action potentials and repetitive spike discharges (Schiffmann et
771 al., 1999; Gall et al., 2003; Bearzatto et al., 2006). Importantly, these calretinin-deficient induced
772 changes are rescued by administering BAPTA, a buffer with fast calcium binding capability,
773 further suggesting that calretinin reduces neuronal excitability via fast calcium binding (Gall et
774 al., 2003). Many neurons in the chicken NMc do not express calretinin and are more excitable,
775 suggesting that the absence of calretinin may contribute to this increased excitability. The
776 chicken NMc contains multiple cell types with differential expressions of calretinin and
777 parvalbumin, providing a useful model for studying expression mechanisms and specific
778 functions of these calcium binding proteins.

779 **CCK in auditory processing and neuronal plasticity**

780 Another important discovery of this study is the characterized CCK expression of NMc2 neurons
781 in chickens. In rat brains, CCK acts as an excitatory neurotransmitter or neuromodulator that can

782 enhance the intrinsic excitability of neurons by either decreasing a cell's permeability to
783 potassium or enhancing a nonselective cation current (Miller et al., 1997; Deng and Lei, 2006;
784 Chung and Moore, 2007, 2009a, b). This function of CCK is consistent with increased intrinsic
785 excitability of CCK-expressing NMc2 neurons as compared to CCK-negative neurons in NMc1
786 and the more rostral portion of NM. Intriguingly, most CCK-expressing neurons in mammals are
787 thought to be GABAergic (Fallon et al., 1983; Somogyi et al., 1984; Seroogy et al., 1988;
788 Doetsch et al., 1993; Kubota and Kawaguchi, 1997; Kawaguchi and Kubota, 1998). While in
789 birds, most CCK-expressing neurons are glutamatergic as evident by co-expression of the
790 glutamatergic cell marker VGLUT2 in chicks (Maekawa et al., 2007) and the lack of
791 colocalization with the GABAergic cell marker GAD65 in the zebra finch (Lovell and Mello,
792 2010). Few GABAergic neurons were reported in the avian NM (Carr et al., 1989; Code et al.,
793 1989), further supporting the notion that CCK-expressing neurons in NMc2 are non-GABAergic.
794 Together, these studies suggest that CCK may act similarly on modulating cellular physiology
795 across various neuronal types in mammalian and avian brains.

796 One possible function of CCK-enhanced neuronal excitability may be related to some
797 aspects of neuronal plasticity and/or integration of multisensory inputs. Local infusion of CCK in
798 the rat auditory cortex potentiates synaptic strength and neuronal responses to auditory stimuli
799 (Li et al., 2014). Interestingly, this plasticity can enable a novel response of these auditory
800 neurons to a visual stimulus after pairing the visual stimulus with a strong auditory stimulus in the
801 presence of CCK (Li et al., 2014). This finding is particularly interesting in light of the
802 distribution of CCK-expressing neurons in the secondary non-lemniscal auditory pathway that is
803 involved in polysensory integration, temporal pattern recognition, and certain forms of learning
804 (Hu, 2003; Lee et al., 2015). Within this pathway, CCK is strongly expressed in the external

805 nucleus of the inferior colliculus (ICx) and thalamic neurons surrounding the medial geniculate
806 body (MGB; Fallon and Seroogy, 1984; Paloff et al., 1996) as well as the avian counterparts
807 (Ball et al., 1988; Lovell and Mello, 2010). In contrast, neurons in the primary lemniscus
808 auditory pathway including the central nucleus of IC (ICc) and MGB do not express CCK,
809 emphasizing specialized function of CCK in sensory processing. Behaviorally, CCK has been
810 proposed to play important roles in visual imprinting in chickens (Maekawa et al., 2007;
811 Nakamori et al., 2013) and probably certain aspects of song processing in zebra finches (Lovell
812 and Mello, 2010). Our observation that CCK is expressed in the chicken NMc2 but not the
813 remaining NM suggests that NMc2 may have additional function other than representing the
814 very low frequency of the tonotopic axis.

815 **Potential mechanisms underlying increased excitability of NMc1 and NMc2 neurons**

816 A characterized intrinsic property of NMc1 and NMc2 neurons is increased excitability as
817 compared to adendritic NM neurons. Consistent with previous studies (Fukui and Ohmori,
818 2004), we found that the majority of NMc1 and NMc2 neurons fire multiple action potentials
819 (APs) in response to relatively weak levels of current injection. We further found that a high
820 percentage of NMc1 and NMc2 neurons (> 67%) show repetitive firing during sustained current
821 injections. A lower percentage (10%) was reported in Fukui and Ohmori (2004) in which neuron
822 sampling did not include the most caudolateral NM where the major body of NMc2 was located
823 (see their Fig. 2). This discrepancy suggests that NMc2 neurons may be more excitable than
824 NMc1 neurons. Alternatively, age differences should be taken into consideration (E20-21 in the
825 current study vs. hatchling in Fukui and Ohmori, 2004).

826 Voltage dependent potassium channels, in particular the low-voltage activated K_{V1}
827 subfamily (Johnston et al., 2010), may be one mechanism that accounts for the higher

828 excitability of NMc1/NMc2 neurons. Compared to the adendritic NM neurons, which have large
829 amounts of K_V1 conductances, the caudolateral NM has a lower level of $K_V1.1$ mRNA staining
830 (Fukui and Ohmori, 2004). In addition, when $K_V1.1$ conductances are blocked, adendritic NM
831 neurons display multiple spikes, resembling the properties of NMc1/NMc2 neurons (Reyes et al.,
832 1994; Rathouz and Trussell, 1998; Hong et al., 2016).

833 In addition to increased excitability, we found that NMc1/NMc2 neurons generate slower
834 and less reliable APs in a heterogeneous manner. In contrast, AP properties of adendritic NM
835 neurons are highly homogeneous, showing faster and highly reliable APs (Hong et al., 2016).
836 The AP fall rate of NMc1/NMc2 neurons is significantly lower than adendritic NM neurons
837 (Hong et al., 2016). It is well known that high-voltage activated K_V3 channels are critical
838 regulators of AP kinetics in the repolarizing phase (Johnston et al., 2010). Blockade of K_V3
839 channels in adendritic NM neurons leads to slower AP generation (Hong et al., 2016). The
840 caudolateral NM expresses weaker K_V3 channel expression than other NM regions
841 (Parameshwaran et al., 2001), suggesting lower levels of K_V3 conductances in NMc1/NMc2
842 neurons, resulting in their slower AP kinetics.

843 **Conclusion**

844 The caudolateral NM at the low frequency end of the tonotopic axis differ from neurons
845 encoding higher frequencies in structure, molecular signaling, and physiology. In addition, the
846 low frequency NM itself is heterogeneous, containing morphologically and potentially
847 functionally distinct neuron types. These results indicate highly specialized and intricate
848 neuronal mechanisms for processing low frequency sounds. Further studies aim to characterize
849 these mechanisms and investigate their contribution to auditory temporal processing and binaural
850 hearing.

851

852 **References**

853 Akemann W, Knopfel T (2006) Interaction of Kv3 potassium channels and resurgent sodium
854 current influences the rate of spontaneous firing of Purkinje neurons. *The Journal of*
855 *neuroscience : the official journal of the Society for Neuroscience* 26:4602-4612.

856

857 Ball GF, Faris PL, Hartman BK, Wingfield JC (1988) Immunohistochemical localization of
858 neuropeptides in the vocal control regions of two songbird species. *J Comp Neurol* 268:171-180.

859

860 Bearzatto B, Servais L, Roussel C, Gall D, Baba-Aissa F, Schurmans S, de Kerchove d'Exaerde
861 A, Cheron G, Schiffmann SN (2006) Targeted calretinin expression in granule cells of calretinin-
862 null mice restores normal cerebellar functions. *FASEB J* 20:380-382.

863

864 Bloom S, Williams A, MacLeod KM (2014) Heterogeneous calretinin expression in the avian
865 cochlear nucleus angularis. *J Assoc Res Otolaryngol* 15:603-620.

866

867 Boord RL, Rasmussen GL (1963) Projection of the cochlear and lagenar nerves on the cochlear
868 nuclei of the pigeon. *J Comp Neurol* 120:463-475.

869

870 Born DE, Durham D, Rubel EW (1991) Afferent influences on brainstem auditory nuclei of the
871 chick: nucleus magnocellularis neuronal activity following cochlea removal. *Brain Res* 557:37-
872 47.

873

874 Burger RM, Cramer KS, Pfeiffer JD, Rubel EW (2005a) Avian superior olivary nucleus provides
875 divergent inhibitory input to parallel auditory pathways. *J Comp Neurol* 481:6-18.

876

877 Burger RM, Fukui I, Ohmori H, Rubel EW (2011) Inhibition in the balance: binaurally coupled
878 inhibitory feedback in sound localization circuitry. *J Neurophysiol* 106:4-14.

879

880 Burger RM, Pfeiffer JD, Westrum LE, Bernard A, Rubel EW (2005b) Expression of GABA(B)
881 receptor in the avian auditory brainstem: ontogeny, afferent deprivation, and ultrastructure. *J*
882 *Comp Neurol* 489:11-22.

883

884 Cant NB, Benson CG (2006) Organization of the inferior colliculus of the gerbil (*Meriones*
885 *unguiculatus*): differences in distribution of projections from the cochlear nuclei and the superior
886 olivary complex. *J Comp Neurol* 495:511-528.

887

888 Carr CE, Konishi M (1990) A circuit for detection of interaural time differences in the brain stem
889 of the barn owl. *J Neurosci* 10:3227-3246.

890

891 Carr CE, Soares D (2002) Evolutionary convergence and shared computational principles in the
892 auditory system. *Brain, behavior and evolution* 59:294-311.

893

894 Carr CE, Fujita I, Konishi M (1989) Distribution of GABAergic neurons and terminals in the
895 auditory system of the barn owl. *J Comp Neurol* 286:190-207.

896

- 897 Chung L, Moore SD (2007) Cholecystokinin enhances GABAergic inhibitory transmission in
898 basolateral amygdala. *Neuropeptides* 41:453-463.
899
- 900 Chung L, Moore SD (2009) Cholecystokinin excites interneurons in rat basolateral amygdala. *J*
901 *Neurophysiol* 102:272-284.
902
- 903 Chung L, Moore SD, Cox CL (2009) Cholecystokinin action on layer 6b neurons in
904 somatosensory cortex. *Brain Res* 1282:10-19.
905
- 906 D'Amico-Martel A (1982) Temporal patterns of neurogenesis in avian cranial sensory and
907 autonomic ganglia. *Am J Anat* 163:351-372.
908
- 909 D'Amico-Martel A, Noden DM (1983) Contributions of placodal and neural crest cells to avian
910 cranial peripheral ganglia. *Am J Anat* 166:445-468.
911
- 912 Dargan SL, Schwaller B, Parker I (2004) Spatiotemporal patterning of IP3-mediated Ca²⁺
913 signals in *Xenopus* oocytes by Ca²⁺-binding proteins. *J Physiol* 556:447-461.
914
- 915 Deng PY, Lei S (2006) Bidirectional modulation of GABAergic transmission by cholecystokinin
916 in hippocampal dentate gyrus granule cells of juvenile rats. *J Physiol* 572:425-442.
917

918 Doetsch GS, Norelle A, Mark EK, Standage GP, Lu SM, Lin RC (1993) Immunoreactivity for
919 GAD and three peptides in somatosensory cortex and thalamus of the raccoon. *Brain Res Bull*
920 31:553-563.

921

922 Fallon JH, Seroogy KB (1984) Visual and auditory pathways contain cholecystokinin: evidence
923 from immunofluorescence and retrograde tracing. *Neurosci Lett* 45:81-87.

924

925 Fallon JH, Wang C, Kim Y, Canepa N, Loughlin S, Seroogy K (1983) Dopamine- and
926 cholecystokinin-containing neurons of the crossed mesostriatal projection. *Neurosci Lett* 40:233-
927 238.

928

929 Franzen DL, Gleiss SA, Berger C, Kumpfbeck FS, Ammer JJ, Felmy F (2015) Development and
930 modulation of intrinsic membrane properties control the temporal precision of auditory brain
931 stem neurons. *J Neurophys* 113:524-536.

932

933 Fukui I, Ohmori H (2004) Tonotopic gradients of membrane and synaptic properties for neurons
934 of the chicken nucleus magnocellularis. *J Neurosci* 24:7514-7523.

935

936 Fukui I, Sato T, Ohmori H (2006) Improvement of phase information at low sound frequency in
937 nucleus magnocellularis of the chicken. *J Neurophysiol* 96:633-641.

938

939 Fukui I, Burger RM, Ohmori H, Rubel EW (2010) GABAergic inhibition sharpens the frequency
940 tuning and enhances phase locking in chicken nucleus magnocellularis neurons. *J Neurosci*
941 30:12075-12083.

942

943 Gall D, Roussel C, Susa I, D'Angelo E, Rossi P, Bearzatto B, Galas MC, Blum D, Schurmans S,
944 Schiffmann SN (2003) Altered neuronal excitability in cerebellar granule cells of mice lacking
945 calretinin. *J Neurosci* 23:9320-9327.

946

947 Gazula VR, Strumbos JG, Mei X, Chen H, Rahner C, Kaczmarek LK (2010) Localization of
948 Kv1.3 channels in presynaptic terminals of brainstem auditory neurons. *J Comp Neurol*
949 518:3205-3220.

950

951 Hackett JT, Jackson H, Rubel EW (1982) Synaptic excitation of the second and third order
952 auditory neurons in the avian brain stem. *Neuroscience* 7:1455-1469.

953

954 Hill EM, Koay G, Heffner RS, Heffner HE (2014) Audiogram of the chicken (*Gallus gallus*
955 domesticus) from 2 Hz to 9 kHz. *J Comp Physiol A Neuroethol Sens Neural Behav Physiol*
956 200:863-870.

957

958 Hong H, Rollman L, Feinstein B, Sanchez JT (2016) Developmental Profile of Ion Channel
959 Specializations in the Avian Nucleus Magnocellularis. *Front Cell Neurosci* 10:80.

960

961 Howard MA, Rubel EW (2010) Dynamic spike thresholds during synaptic integration preserve
962 and enhance temporal response properties in the avian cochlear nucleus. *J Neurosci* 30:12063-
963 12074.

964

965 Howard MA, Burger RM, Rubel EW (2007) A developmental switch to GABAergic inhibition
966 dependent on increases in Kv1-type K⁺ currents. *The Journal of neuroscience : the official*
967 *journal of the Society for Neuroscience* 27:2112-2123.

968

969 Hu B (2003) Functional organization of lemniscal and nonlemniscal auditory thalamus. *Exp*
970 *Brain Res* 153:543-549.

971

972 Jhaveri S, Morest DK (1982) Sequential alterations of neuronal architecture in nucleus
973 magnocellularis of the developing chicken: a Golgi study. *Neuroscience* 7:837-853.

974

975 Johnston J, Forsythe ID, Kopp-Scheinflug C (2010) Going native: voltage-gated potassium
976 channels controlling neuronal excitability. *The Journal of physiology* 588:3187-3200.

977

978 Kaiser A, Manley GA (1996) Brainstem connections of the macula lagenae in the chicken. *J*
979 *Comp Neurol* 374:108-117.

980

981 Kaneko T, Ye B (2015) Fine-scale topography in sensory systems: insights from *Drosophila* and
982 vertebrates. *J Comp Physiol A Neuroethol Sens Neural Behav Physiol* 201:911-920.

983

- 984 Kawaguchi Y, Kubota Y (1998) Neurochemical features and synaptic connections of large
985 physiologically-identified GABAergic cells in the rat frontal cortex. *Neuroscience* 85:677-701.
986
- 987 Kirsch J, Wolters I, Triller A, Betz H (1993) Gephyrin antisense oligonucleotides prevent
988 glycine receptor clustering in spinal neurons. *Nature* 366:745-748.
989
- 990 Koppl C (1994) Auditory nerve terminals in the cochlear nucleus magnocellularis: differences
991 between low and high frequencies. *J Comp Neurol* 339:438-446.
992
- 993 Koppl C, Carr CE (1997) Low-frequency pathway in the barn owl's auditory brainstem. *J Comp*
994 *Neurol* 378:265-282.
995
- 996 Kubke MF, Gauger B, Basu L, Wagner H, Carr CE (1999) Development of calretinin
997 immunoreactivity in the brainstem auditory nuclei of the barn owl (*Tyto alba*). *J Comp Neurol*
998 415:189-203.
999
- 1000 Kubota Y, Kawaguchi Y (1997) Two distinct subgroups of cholecystokinin-immunoreactive
1001 cortical interneurons. *Brain Res* 752:175-183.
1002
- 1003 Leao RN, Sun H, Svahn K, Berntson A, Youssoufian M, Paolini AG, Fyffe RE, Walmsley B
1004 (2006) Topographic organization in the auditory brainstem of juvenile mice is disrupted in
1005 congenital deafness. *J Physiol* 571:563-578.
1006

- 1007 Lee CC (2015) Exploring functions for the non-lemniscal auditory thalamus. *Front Neural*
1008 *Circuits* 9:69.
1009
- 1010 Lewis AH, Raman IM (2014) Resurgent current of voltage-gated Na(+) channels. *The Journal of*
1011 *physiology* 592:4825-4838.
1012
- 1013 Li J, Zhou X, Huang L, Fu X, Liu J, Zhang X, Sun Y, Zuo M (2013) Alteration of CaBP
1014 expression pattern in the nucleus magnocellularis following unilateral cochlear ablation in adult
1015 zebra finches. *PLoS One* 8:e79297.
1016
- 1017 Li X, Yu K, Zhang Z, Sun W, Yang Z, Feng J, Chen X, Liu CH, Wang H, Guo YP, He J (2014)
1018 Cholecystokinin from the entorhinal cortex enables neural plasticity in the auditory cortex. *Cell*
1019 *Res* 24:307-330.
1020
- 1021 Lim R, Alvarez FJ, Walmsley B (2000) GABA mediates presynaptic inhibition at glycinergic
1022 synapses in a rat auditory brainstem nucleus. *J Physiol* 525 Pt 2:447-459.
1023
- 1024 Lovell PV, Mello CV (2011) Brain expression and song regulation of the cholecystokinin gene
1025 in the zebra finch (*Taeniopygia guttata*). *J Comp Neurol* 519:211-237.
1026
- 1027 MacLeod KM, Carr CE (2007) Beyond timing in the auditory brainstem: intensity coding in the
1028 avian cochlear nucleus angularis. *Progress in brain research* 165:123-133.
1029

1030 MacLeod KM, Soares D, Carr CE (2006) Interaural timing difference circuits in the auditory
1031 brainstem of the emu (*Dromaius novaehollandiae*). *J Comp Neurol* 495:185-201.
1032

1033 Maekawa F, Nakamori T, Uchimura M, Fujiwara K, Yada T, Tsukahara S, Kanamatsu T, Tanaka
1034 K, Ohki-Hamazaki H (2007) Activation of cholecystokinin neurons in the dorsal pallium of the
1035 telencephalon is indispensable for the acquisition of chick imprinting behavior. *J Neurochem*
1036 102:1645-1657.
1037

1038 Miller KK, Hoffer A, Svoboda KR, Lupica CR (1997) Cholecystokinin increases GABA release
1039 by inhibiting a resting K⁺ conductance in hippocampal interneurons. *J Neurosci* 17:4994-5003.
1040

1041 Moerel M, De Martino F, Formisano E (2014) An anatomical and functional topography of
1042 human auditory cortical areas. *Front Neurosci* 8:225.
1043

1044 Nakamori T, Maekawa F, Sato K, Tanaka K, Ohki-Hamazaki H (2013) Neural basis of
1045 imprinting behavior in chicks. *Dev Growth Differ* 55:198-206.
1046

1047 Neil MA, Juskaitis R, Wilson T (1997) Method of obtaining optical sectioning by using
1048 structured light in a conventional microscope. *Opt Lett* 22:1905-1907.
1049

1050 Neil MA, Squire A, Juskaitis R, Bastiaens PI, Wilson T (2000) Wide-field optically sectioning
1051 fluorescence microscopy with laser illumination. *J Microsc* 197:1-4.
1052

- 1053 Nejatbakhsh N, Feng ZP (2011) Calcium binding protein-mediated regulation of voltage-gated
1054 calcium channels linked to human diseases. *Acta Pharmacol Sin* 32:741-748.
1055
- 1056 Oertel D (1983) Synaptic responses and electrical properties of cells in brain slices of the mouse
1057 anteroventral cochlear nucleus. *The Journal of neuroscience : the official journal of the Society*
1058 *for Neuroscience* 3:2043-2053.
1059
- 1060 Oertel D (1985) Use of brain slices in the study of the auditory system: spatial and temporal
1061 summation of synaptic inputs in cells in the anteroventral cochlear nucleus of the mouse. *J*
1062 *Acoust Soc Am* 78:328-333.
1063
- 1064 Oertel D (1997) Encoding of timing in the brain stem auditory nuclei of vertebrates. *Neuron*
1065 19:959-962.
1066
- 1067 Oline SN, Burger RM (2014) Short-term synaptic depression is topographically distributed in the
1068 cochlear nucleus of the chicken. *J Neurosci* 34:1314-1324.
1069
- 1070 Oline SN, Ashida G, Burger RM (2016) Tonotopic Optimization for Temporal Processing in the
1071 Cochlear Nucleus. *J Neurosci* 36:8500-8515.
1072
- 1073 Oyler GA, Higgins GA, Hart RA, Battenberg E, Billingsley M, Bloom FE, Wilson MC (1989)
1074 The identification of a novel synaptosomal-associated protein, SNAP-25, differentially expressed
1075 by neuronal subpopulations. *J Cell Biol* 109:3039-3052.

1076

1077 Paloff AM, Vankova ME, Hinova-Palova DV (1996) Cholecystokinin-like immunoreactivity in
1078 cat inferior colliculus. Light and ultrastructural study. *J Hirnforsch* 37:467-478.

1079

1080 Parameshwaran S, Carr CE, Perney TM (2001) Expression of the Kv3.1 potassium channel in
1081 the avian auditory brainstem. *The Journal of neuroscience : the official journal of the Society for*
1082 *Neuroscience* 21:485-494.

1083

1084 Parks TN, Rubel EW (1978) Organization and development of the brain stem auditory nuclei of
1085 the chicken: primary afferent projections. *J Comp Neurol* 180:439-448.

1086

1087 Parks TN, Code RA, Taylor DA, Solum DA, Strauss KI, Jacobowitz DM, Winsky L (1997)
1088 Calretinin expression in the chick brainstem auditory nuclei develops and is maintained
1089 independently of cochlear nerve input. *J Comp Neurol* 383:112-121.

1090

1091 Raman IM, Bean BP (1999) Ionic currents underlying spontaneous action potentials in isolated
1092 cerebellar Purkinje neurons. *The Journal of neuroscience : the official journal of the Society for*
1093 *Neuroscience* 19:1663-1674.

1094

1095 Rathouz M, Trussell L (1998) Characterization of outward currents in neurons of the avian
1096 nucleus magnocellularis. *Journal of neurophysiology* 80:2824-2835.

1097

- 1098 Rebillard G, Rubel EW (1981) Electrophysiological study of the maturation of auditory
1099 responses from the inner ear of the chick. *Brain Res* 229:15-23.
1100
- 1101 Reyes AD, Rubel EW, Spain WJ (1994) Membrane properties underlying the firing of neurons in
1102 the avian cochlear nucleus. *The Journal of neuroscience : the official journal of the Society for*
1103 *Neuroscience* 14:5352-5364.
1104
- 1105 Rogers JH (1987) Calretinin: a gene for a novel calcium-binding protein expressed principally in
1106 neurons. *J Cell Biol* 105:1343-1353.
1107
- 1108 Rogers JH (1989) Two calcium-binding proteins mark many chick sensory neurons.
1109 *Neuroscience* 31:697-709.
1110
- 1111 Rubel EW, Parks TN (1975) Organization and development of brain stem auditory nuclei of the
1112 chicken: tonotopic organization of n. magnocellularis and n. laminaris. *J Comp Neurol* 164:411-
1113 433.
1114
- 1115 Rubel EW, Fritsch B (2002) Auditory system development: primary auditory neurons and their
1116 targets. *Annu Rev Neurosci* 25:51-101.
1117
- 1118 Ryugo DK, Parks TN (2003). Primary innervation of the avian and mammalian cochlear nucleus.
1119 *Brain Res Bull.* 60(5-6):435-56.
1120

- 1121 Safieddine S, Wenthold RJ (1999) SNARE complex at the ribbon synapses of cochlear hair cells:
1122 analysis of synaptic vesicle- and synaptic membrane-associated proteins. *Eur J Neurosci* 11:803-
1123 812.
1124
- 1125 Sanchez JT, Quinones K, Otto-Meyer S (2015a) Factors Influencing Short-term Synaptic
1126 Plasticity in the Avian Cochlear Nucleus Magnocellularis. *J Exp Neurosci* 9:11-24.
1127
- 1128 Sanchez JT, Ghelani S, Otto-Meyer S (2015b) From development to disease: diverse functions of
1129 NMDA-type glutamate receptors in the lower auditory pathway. *Neuroscience* 285:248-259.
1130
- 1131 Sanchez JT, Wang Y, Rubel EW, Barria A (2010) Development of glutamatergic synaptic
1132 transmission in binaural auditory neurons. *J Neurophysiol* 104:1774-1789.
1133
- 1134 Sanchez JT, Seidl AH, Rubel EW, Barria A (2011) Preparation and culture of chicken auditory
1135 brainstem slices. *Journal of visualized experiments : JoVE*.
1136
- 1137 Sanchez JT, Seidl AH, Rubel EW, Barria A (2012a) Control of neuronal excitability by NMDA-
1138 type glutamate receptors in early developing binaural auditory neurons. *J Physiol* 590:4801-
1139 4818.
1140
- 1141 Sanchez JT, Seidl AH, Rubel EW, Barria A (2012b) Control of neuronal excitability by NMDA-
1142 type glutamate receptors in early developing binaural auditory neurons. *The Journal of*
1143 *physiology* 590:4801-4818.

1144

1145 Saunders JC, Gates GR, Coles RB (1974) Brain-stem evoked responses as an index of hearing
1146 thresholds in one-day-chicks and ducklings. *J Comp Physiol Psychol* 86:426-431.

1147

1148 Schiffmann SN, Cheron G, Lohof A, d'Alcantara P, Meyer M, Parmentier M, Schurmans S
1149 (1999) Impaired motor coordination and Purkinje cell excitability in mice lacking calretinin.
1150 *Proc Natl Acad Sci U S A* 96:5257-5262.

1151

1152 Schurmans S, Schiffmann SN, Gurden H, Lemaire M, Lipp HP, Schwam V, Pochet R, Imperato
1153 A, Bohme GA, Parmentier M (1997) Impaired long-term potentiation induction in dentate gyrus
1154 of calretinin-deficient mice. *Proc Natl Acad Sci U S A* 94:10415-10420.

1155

1156 Seroogy K, Ceccatelli S, Schalling M, Hokfelt T, Frey P, Walsh J, Dockray G, Brown J, Buchan
1157 A, Goldstein M (1988) A subpopulation of dopaminergic neurons in rat ventral mesencephalon
1158 contains both neurotensin and cholecystokinin. *Brain Res* 455:88-98.

1159

1160 Slee SJ, Higgs MH, Fairhall AL, Spain WJ (2010) Tonotopic tuning in a sound localization
1161 circuit. *J Neurophysiol* 103:2857-2875.

1162

1163 Somogyi P, Hodgson AJ, Smith AD, Nunzi MG, Gorio A, Wu JY (1984) Different populations
1164 of GABAergic neurons in the visual cortex and hippocampus of cat contain somatostatin- or
1165 cholecystokinin-immunoreactive material. *J Neurosci* 4:2590-2603.

1166

- 1167 Stack KE, Code RA (2000) Calretinin expression in the chick cochlear nucleus after
1168 deafferentation. *Brain Res* 873:135-139.
- 1169
- 1170 Sullivan WE, Konishi M (1984) Segregation of stimulus phase and intensity coding in the
1171 cochlear nucleus of the barn owl. *J Neurosci* 4:1787-1799.
- 1172
- 1173 Takahashi TT, Konishi M (1988) Projections of the cochlear nuclei and nucleus laminaris to the
1174 inferior colliculus of the barn owl. *J Comp Neurol* 274:190-211.
- 1175
- 1176 Takahashi TT, Carr CE, Brecha N, Konishi M (1987) Calcium binding protein-like
1177 immunoreactivity labels the terminal field of nucleus laminaris of the barn owl. *J Neurosci*
1178 7:1843-1856.
- 1179
- 1180 Tang ZQ, Dinh EH, Shi W, Lu Y (2011) Ambient GABA-activated tonic inhibition sharpens
1181 auditory coincidence detection via a depolarizing shunting mechanism. *J Neurosci* 31:6121-
1182 6131.
- 1183
- 1184 Tang ZQ, Liu YW, Shi W, Dinh EH, Hamlet WR, Curry RJ, Lu Y (2013) Activation of synaptic
1185 group II metabotropic glutamate receptors induces long-term depression at GABAergic synapses
1186 in CNS neurons. *J Neurosci* 33:15964-15977.
- 1187
- 1188 Trussell LO (1999) Synaptic mechanisms for coding timing in auditory neurons. *Annu Rev*
1189 *Physiol* 61:477-496.

1190

1191 von Bartheld CS, Code RA, Rubel EW (1989) GABAergic neurons in brainstem auditory nuclei
1192 of the chick: distribution, morphology, and connectivity. *J Comp Neurol* 287:470-483.

1193

1194 von Hehn CA, Bhattacharjee A, Kaczmarek LK (2004) Loss of Kv3.1 tonotopicity and
1195 alterations in cAMP response element-binding protein signaling in central auditory neurons of
1196 hearing impaired mice. *J Neurosci* 24:1936-1940.

1197

1198 Wang LC, Tang ZQ, Lu Y (2012) Synaptic activity-induced Ca(2+) signaling in avian cochlear
1199 nucleus magnocellularis neurons. *Neurosci Res* 72:129-139.

1200

1201 Wang Y, Rubel EW (2012) In vivo reversible regulation of dendritic patterning by afferent input
1202 in bipolar auditory neurons. *J Neurosci* 32:11495-11504.

1203

1204 Wang Y, Cunningham DE, Tempel BL, Rubel EW (2009) Compartment-specific regulation of
1205 plasma membrane calcium ATPase type 2 in the chick auditory brainstem. *J Comp Neurol*
1206 514:624-640.

1207

1208 Warchol ME, Dallos P (1990) Neural coding in the chick cochlear nucleus. *J Comp Physiol A*
1209 166:721-734.

1210

1211 **Tables**1212 **Table 1. Primary antibodies used for immunostaining.**

Antibody	Manufacturer	RRID	Host species	Working concentration
Calretinin	Millipore; AB5054	AB_2068506	Rabbit	1:5000
CCK	Sigma; C2581	AB_258806	Rabbit	1:2000
CTB	List Biological Lab; 703	AB_2636895 (temporary)	Goat	1:12000
Gephyrin	Synaptic Systems; mAb7a	AB_2314591	Mouse	1:500
MAP2	Millipore; MAB3418	AB_94856	Mouse	1:1000
Parvalbumin	Sigma; P3088	AB_477329	Mouse	1:5000
SNAP25	Millipore; MAB331	AB_94805	Mouse	1:1000

1213 Abbreviations: CCK, Cholecystokinin; CTB, Cholera toxin B; MAP2, microtubule-associated

1214 protein 2; SNAP25, synaptosome associated protein 25.

1215

1216

1217 **Table 2. Comparison of passive membrane and action potential (AP) properties between**
 1218 **NMc1/NMc2 and mid- to high-CF NM neurons**

Properties	NMc1 / NMc2	Mid- to High-CF NM*	T-test <i>P</i>
Passive membrane properties			
RMP (mV) [#]	-50.55 ± 9.74 (30)	-66.52 ± 8.49 (28)	<i>P</i> < 0.0001
Time constant tau (ms)	20.39 ± 17.25 (29)	3.18 ± 1.33 (20)	<i>P</i> < 0.0001
Input resistance (MΩ)	467.2 ± 342.5 (29)	123.90 ± 49.90 (20)	<i>P</i> < 0.0001
Membrane capacitance (pF)	41.25 ± 21.74 (29)	26.15 ± 4.60 (20)	<i>P</i> < 0.01
Action potential properties			
Threshold current (pA)	38.96 ± 25.96 (22)	321.70 ± 121.00 (28)	<i>P</i> < 0.0001
Max rise rate (mV/ms) [§]	136.1 ± 41.01 (22)	155.60 ± 42.19 (28)	<i>P</i> = 0.107
Max fall rate (mV/ms) [§]	-69.14 ± 22.16 (22)	-104.40 ± 29.79 (28)	<i>P</i> < 0.0001
AP half width (ms) [§]	1.45 ± 0.48 (22)	0.97 ± 0.17 (28)	<i>P</i> < 0.0001
AP reliability range (ms) [§]	6.98 ± 5.87 (17) [^]	0.21 ± 0.14 (28)	<i>P</i> < 0.0001

1219 CF = Characteristic frequency. RMP = Resting membrane potential. * = Data from Hong et al.,
 1220 2016. Experimental conditions (e.g., temperature) and recording parameters (e.g., membrane
 1221 capacitance) for both studies are the same. [#] = Numeric values without the correction of -10 mV
 1222 junction potential. [§] = Measured from APs in response to current injections 25% above threshold
 1223 current. [^] = Five outlier neurons with reliability range > 30 ms were removed. Number in
 1224 parentheses = n.

1225 **Figure Legends**

1226 **Figure 1: Three subdivisions of the caudal NM revealed by MAP2 immunoreactivity. A-D:**
1227 Low-magnification images taken from the caudomost (A), caudal (B), middle (C), and rostral
1228 (D) regions of NM at the coronal plane. To visualize MAP2 staining in NM, the images were
1229 saturated in the surrounding tissues that are stained more strongly for MAP2 immunoreactivity
1230 than NM and NL. Dashed lines outline the border of NM. **E-H:** High-magnification images of
1231 the caudolateral NM. Dashed white and yellow lines outline the border of NMc1 and NMc2,
1232 respectively. Images in E and F were taken from the level between A and B. Image in G was
1233 taken from the same section in B, while the image in H is at a level slightly rostral to B and G.
1234 Note distinct staining pattern of MAP2 between NMcm, NMc1, and NMc2. For each image,
1235 right is lateral and up is dorsal. **I:** The relative location of NMc1 and NMc2 along the caudal-
1236 rostral axis in series coronal sections through NM. Abbreviations: l, lateral; d, dorsal; NM,
1237 nucleus magnocellularis; NMcm, caudomedial NM; NMc1, caudolateral NM subregion 1;
1238 NMc2, caudolateral NM subregion 2. Scale bars = 200 μm in D (applies to A-D) and 100 μm in
1239 H (applies to E-H).

1240

1241 **Figure 2: Comparison of neuronal cell body size in NMcm, NMc1, and NMc2. A-C:**
1242 NeuroTrace stain in NMcm (A), NMc1 (B), and NMc2 (C) on coronal sections. White dashed
1243 circles illustrate examples of measured neurons. **D:** Low-power image of MAP2 immunostaining
1244 on the section containing the three subregions. The NMc1 is outlined with dashed line. **E:**
1245 Projection of 3D color map surface plot representing the somatic area of NM neurons in relation
1246 to their location on the section shown in D. Warm colors represent larger cells. The NMc1 in D
1247 is indicated accordingly by dashed line. An arrow indicates a group of large cells along the

1248 lateral edge of NMc2. **F:** Bar chart of the cross-sectional somatic areas in NMcm, NMc1 and
1249 NMc2. *** indicates significant difference ($P < 0.001$). Data are presented as mean \pm SD.
1250 Abbreviations: see Figure 1. Scale bar = 20 μ m in C (applies to A-C) and 100 μ m in D.

1251

1252 **Figure 3: Single cell dye-filling shows different dendritic morphology in NMcm, NMc1 and**
1253 **NMc2.** **A:** An example slice containing several filled neurons in different subregions along the
1254 lateral-to-medial axis. The black dashed circle outlines NM. Cell bodies of the filled neurons
1255 (red) are evident in this low magnification image. **B-D:** Higher magnification of the boxes in A
1256 showing maximum z-projection of filled neurons in NMc2 (B), NMc1 (C), and NMcm (D). **E-F:**
1257 3D reconstruction of the filled neurons in B. **G:** 3D reconstruction of the filled neurons in C. **H:**
1258 3D reconstruction of the filled neuron in D. **I:** Quantitative analysis of the total dendritic branch
1259 length. **J:** Quantitative analysis of the number of primary trees. *** indicates $P < 0.001$; **
1260 indicates $P < 0.01$; * indicates $P < 0.05$. Data are presented as mean \pm SD. Abbreviations: see
1261 Figure 1. Scale bars = 200 μ m in A; and 20 μ m in H (applies to B-H).

1262

1263 **Figure 4: CCK is a biomarker for NMc2.** The left (A1, B1, C1, D1) and middle (A2, B2, C2,
1264 D2) columns are MAP2 and CCK immunostaining, respectively. The right column (A3, B3, C3,
1265 and D3) shows the merged images. **A-C:** Low-magnification images were taken from sections
1266 located caudal to rostral from the same animal. Dashed lines outline NMc1. Arrows in B2
1267 indicate CCK positive neurons in NMc1. **D:** High-magnification images of the box in A3.
1268 Arrows and arrowheads indicate darkly and lightly CCK labeled NMc2 neurons, respectively. **E:**
1269 Bar chart of the mean gray scale of CCK expressing neurons in NMcm, NMc1 and NMc2. **F:**
1270 Bar chart of the percentage of CCK immunoreactive neurons in NMcm, NMc1 and NMc2. *

1271 indicates $P < 0.05$, ** indicates $P < 0.01$, *** indicates $P < 0.001$, and ns indicates no significance.
1272 Data are presented as mean \pm SD. Abbreviations: see Figure 1. Scale bars = 100 μm in C3
1273 (applies to A1-C3); 20 μm in D3 (applies to D1-D3).
1274
1275 **Figure 5: NMc1 and NMc2 receive excitatory inputs from auditory nerve fibers. A:**
1276 Schematic drawing shows injection sites of BDA in auditory and vestibular branches of the 8th
1277 nerve. See details in Methods. **B:** The injection site (white arrow) in the cochlear branch outlined
1278 by dashed lines. **C:** BDA labeled axons and terminals in NMcm. The inset shows the end-bulb
1279 morphology of a labeled terminal. **D:** BDA labeled axons and terminals in NMc1 and NMc2.
1280 The images were taken from a section at the level of Fig. 1E. The inset shows the bouton-like
1281 morphology of labeled terminals. **E-H:** BDA labeled axons and terminals in NMcm, NMc1, and
1282 NMc2 at the level of Fig. 1F. NMc1 is outlined by dashed line. F-H are the closer views of
1283 NMcm (F), NMc1 (G), NMc2 (H). **I-L:** Double labeling of BDA (green) and the excitatory
1284 synaptic marker SNAP25 (magenta). J-L are the closer views of NMcm (J), NMc1 (K), NMc2
1285 (L). Arrows in J indicate a number of BDA labeled end-bulbs double stained with SNAP25. **M:**
1286 No labeling was observed in vestibular nuclei following injections in the cochlear branch. **N:** The
1287 injection site (white arrow) in the vestibular branch outlined by dashed lines. **O:** No labeling in
1288 NM following the injection in N. **P:** BDA labeled terminals in the vestibular nucleus ventral to
1289 NM. Inset shows a labeled terminal around a vestibular neuron. Abbreviations: BDA, dextran;
1290 NeuT, NeuroTrace; Ve, vestibular nucleus; NA, nucleus angularis; NL, nucleus laminaris. Other
1291 abbreviations see Figure 1. Scale bars = 100 μm in B, M, N, O, and P; 50 μm in C-D; 100 μm in
1292 I (applies to E and I); 20 μm in L (applies to F-H and J-L); 10 μm in insets.
1293

1294 **Figure 6: NMc1 and NMc2 receive inhibitory inputs from SON.** **A-D:** The distribution
1295 pattern of inhibitory synaptic marker gephyrin. NMc1 is outlined by dashed line. B-D are high-
1296 magnification observations of NMcm (B), NMc1 (C), and NMc2 (D), respectively; **E-H:**
1297 Anterogradely labeled axonal terminals in the caudal NM following an *in vivo* injection of CTB
1298 into SON. Dashed lines outline NMc1 and NMc2. F-H are high-magnification observations of
1299 NMcm (F), NMc1 (G), and NMc2 (H), respectively; **I:** Immunostaining of CCK performed on
1300 the adjacent section of E for identifying NMc2. **J:** Labeled axonal terminals in NM at the level
1301 more rostral than NMc. **K-L:** Labeled cell bodies and neuropil in NL (K) and NA (L). **M:**
1302 Injection site in SON. White dashed line indicates the approximate border of the SON. The
1303 midline is indicated by black dashed line. Abbreviations: CTB, cholera toxin B; SON, superior
1304 olivary nucleus. Other abbreviations see Figure 1. Scale bars = 100 μm in A, E, I; 50 μm in L
1305 (applies to J-L); 20 μm in B (applies to B-D) and H (applies to F-H); 500 μm in M.

1306

1307 **Figure 7: Differential expression of calretinin in the caudal NM.** The left (A1, B1, C1, D1)
1308 and middle (A2, B2, C2, D2) columns are MAP2 and calretinin immunostaining, respectively.
1309 The right column (A3, B3, C3, and D3) are the merged images. **A:** Low-magnification images
1310 were taken from a section at the level of Fig. 1G. **B-D:** High-magnification images of the boxes
1311 in A1. All images were collected with the same imaging parameters and processed in the same
1312 way, except for the inset in D2 in which the brightness is enhanced to show a weakly labeled
1313 neuron in NMc2. Note calretinin expressing neurons in NMcm and NMc1, but not NMc2. The
1314 border between NMc1 and NMc2 is indicated by dashed lines in D. **E:** Bar chart of the ratio of
1315 calretinin expressing neurons in NMcm, NMc1 and NMc2. *** indicates $P < 0.001$. Data are
1316 presented as mean \pm SD. Abbreviations: see Figure 1. Scale bars = 100 μm in A3 (applies to A1-

1317 A3), and 20 μm in D3 (applies to B1-D3).

1318

1319 **Figure 8: Differential expression of parvalbumin in the caudal NM.** The left (A1, B1, C1,
1320 D1) and middle (A2, B2, C2, D2) columns are MAP2 and parvalbumin immunostaining,
1321 respectively. The right column (A3, B3, C3, and D3) are the merged images. **A:** Low-
1322 magnification images were taken from a section at the level of Fig. 1G. **B-D:** High-magnification
1323 images of the boxes in A1. All images were collected with the same imaging parameters and
1324 processed in the same way. Arrows and arrowheads in B-D indicate unlabeled and labeled
1325 somata for parvalbumin. The border between NMc1 and NMc2 is indicated by dashed lines in D.
1326 **E:** Bar chart of the ratio of parvalbumin expressing neurons in NMcm, NMc1 and NMc2. ***
1327 indicates $P < 0.001$, and ns indicates no significance. Data are presented as mean \pm SD.
1328 Abbreviations: see Figure 1. Scale bars = 100 μm in A3 (applies to A1-A3), and 50 μm in D3
1329 (applies to B1-D3).

1330

1331 **Figure 9: Electrophysiological protocols applied to NMc1 and NMc2 neurons. A:**
1332 Neurobiotin labeled NMc1/NMc2 neuron. Inset shows low-magnification image of the entire
1333 coronal NM region with the labeled NMc1/NMc2 neuron. Dorsal = top, lateral = right. Scale bar
1334 = 20 μm (200 μm in inset). **B:** Current clamp protocol to measure passive membrane properties.
1335 Upper trace shows the representative voltage response (average of 30 repetitive trials) recorded
1336 from an NMc1/NMc2 neuron in response to a hyperpolarizing current injection (lower trace, -10
1337 pA). A single exponential was fit to a 30 ms time window following the current injection
1338 (superimposed red line), in order to calculate time constant (τ), input resistance and membrane
1339 capacitance. **C:** Population data showing membrane capacitance (C_{MEMBRANE}) sampled from the

1340 first (also referred as caudmost, Caud-Mos) slice, second/third slices (Caud) and middle to
1341 rostral slices (Mid-Ros, mid- to high-frequency NM, data modified from Hong et al., 2016).
1342 Asterisk represents significance at $p < 0.05$. Error bars = standard error. **D:** Metrics used to
1343 measure action potential (AP) properties. Representative first APs (30 superimposed trials) were
1344 recorded from an NMc1/NMc2 neuron in response to current injections with the strength 25%
1345 above the threshold current (duration = 100 ms). Several AP properties were characterized: rise
1346 rate (A), fall rate (B), half width (C) and reliability range (D). Population data of AP properties
1347 are shown in the corresponding figures in Fig. 11.

1348

1349 **Figure 10: Heterogeneous voltage responses to current injections recorded from NMc1 and**
1350 **NMc2 neurons. A, B and C top:** Upper panel shows representative voltage responses recorded
1351 from three NMc1/NMc2 neurons to current injections from -100 to +80 pA in a step of 20 pA
1352 (lower panel). **A, B and C middle:** Upper panel shows representative voltage responses (30
1353 superimposed trials) recorded from the same three NMc1/NMc2 neurons shown in the top panel,
1354 respectively. Lower panel shows current injections with the strength 25% above threshold
1355 current. Arrowhead in A shows widespread action potential (AP) peak occurrences for this
1356 neuron. Arrow in A shows spontaneous activity. Insets in B and C show the enlargement of 30
1357 superimposed APs. **A, B and C bottom:** Upper panel shows representative voltage responses
1358 recorded from three NMc1/NMc2 neurons to current injections with the strength of 200 pA (A &
1359 B, lower panel) or 500 pA (C, lower panel). **D:** Population data showing the number of APs
1360 elicited as a function of current injections from 0 to 200 pA, step of 20 pA. NMc1/NMc2
1361 neurons are divided into three subgroups: neurons displaying voltage responses similar with the
1362 neurons shown in A, B and C are noted as A-like, B-like and C-like, respectively (see Results for

1363 objective classification details). Mid- to high frequency NM neurons (M-HF) are also shown as a
1364 reference (data modified from Hong et al., 2016). **E-F:** Population data showing resting
1365 membrane potential (RMP, **E**) and input resistance (**F**) of A-like, B-like and C-like NMc1/NMc2
1366 neurons. The duration of all current injections in this figure is 100 ms. Error bars = standard
1367 error.

1368

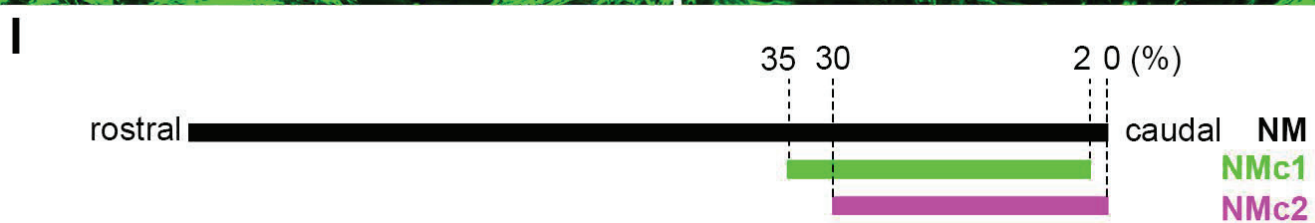
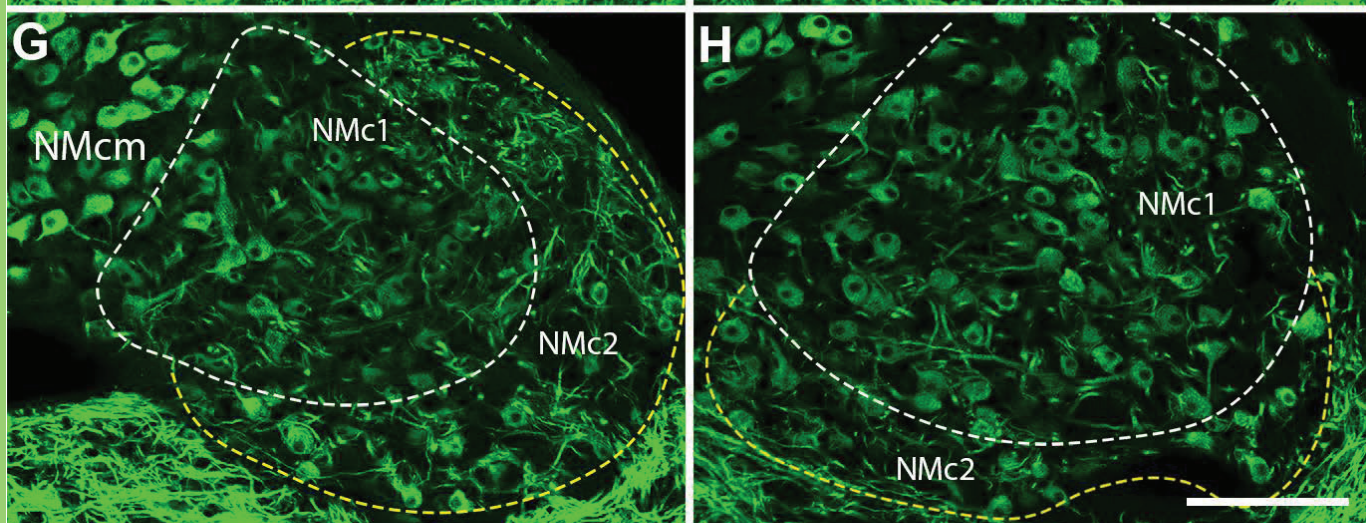
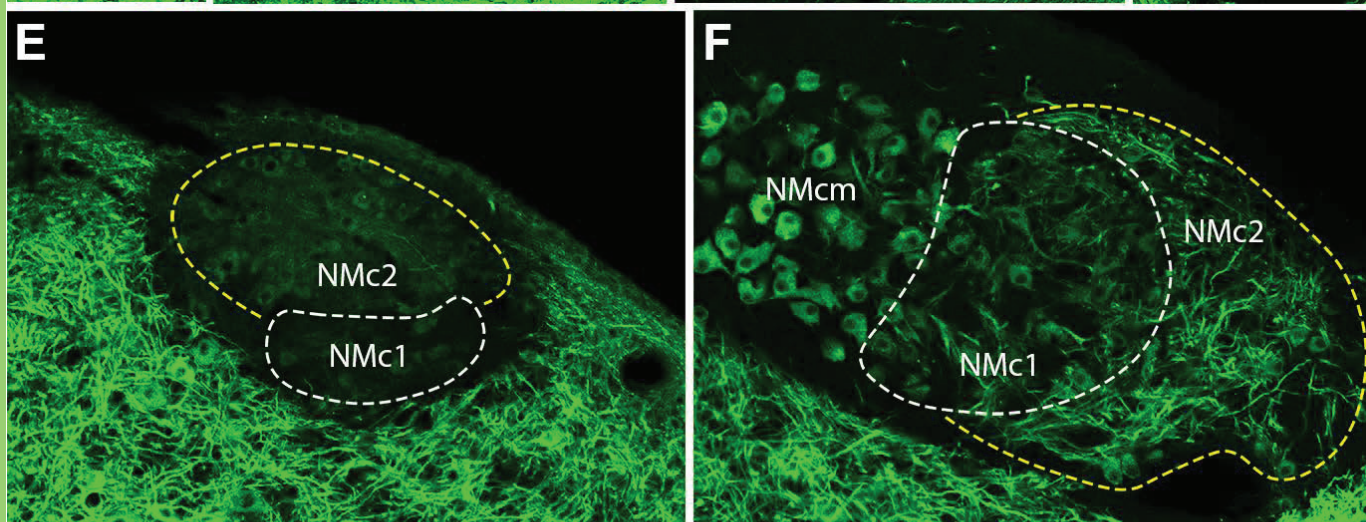
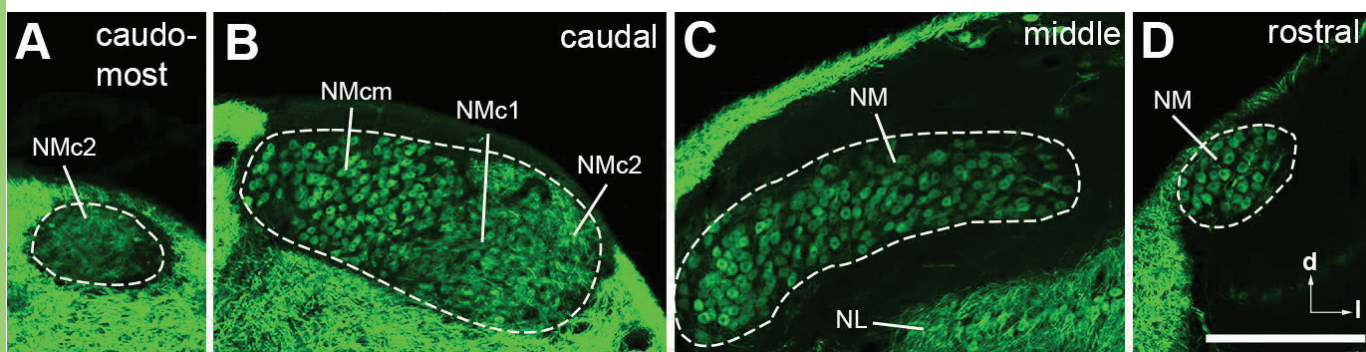
1369 **Figure 11: Heterogeneity of action potential (AP) properties of NMc1 and NMc2 neurons.**

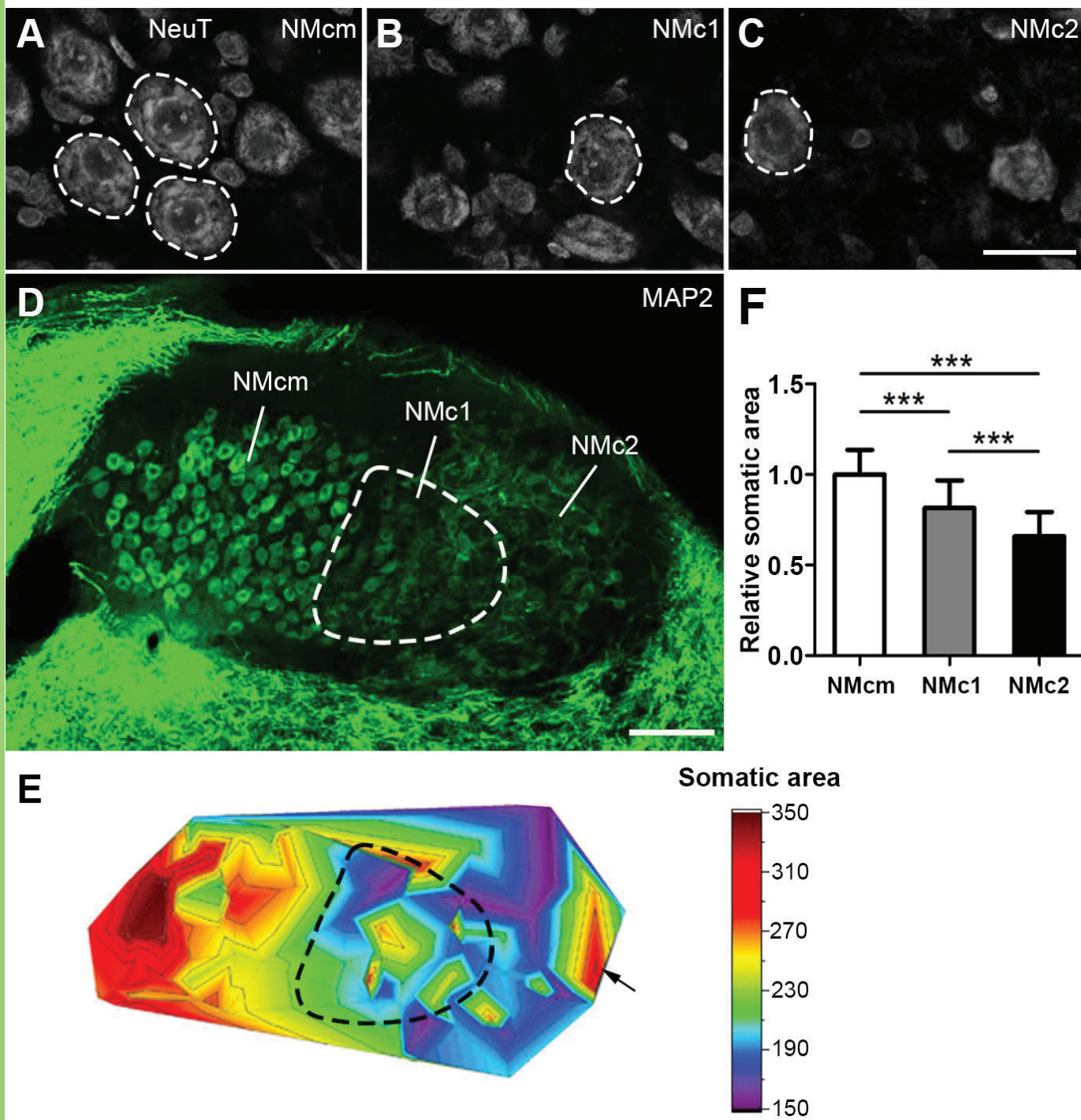
1370 **A:** The number of APs generated in response to 200 pA current injections plotted as a function
1371 of threshold current for individual NMc1/NMc2 neurons. Three filled and labeled circles
1372 represent the neurons shown in Fig. 10A, B and C, respectively. Correlation coefficient r and p
1373 values are shown. **B-C:** Threshold current plotted as a function of membrane capacitance (**B**) and
1374 input resistance (**C**) for individual NMc1/NMc2 neurons. **D-G:** Population data of AP rise rate
1375 (**D**), fall rate (**E**), half width (**F**) and reliability range (**G**) are plotted for individual NMc1/NMc2
1376 neurons, as a function of threshold current (left), membrane capacitance (middle) and input
1377 resistance (right). Correlation coefficient r and p values are shown. Three filled circles represent
1378 the neurons shown in Fig. 10A, B and C, respectively. Note that in G, five outliers with
1379 extremely large range (> 30 ms) were removed.

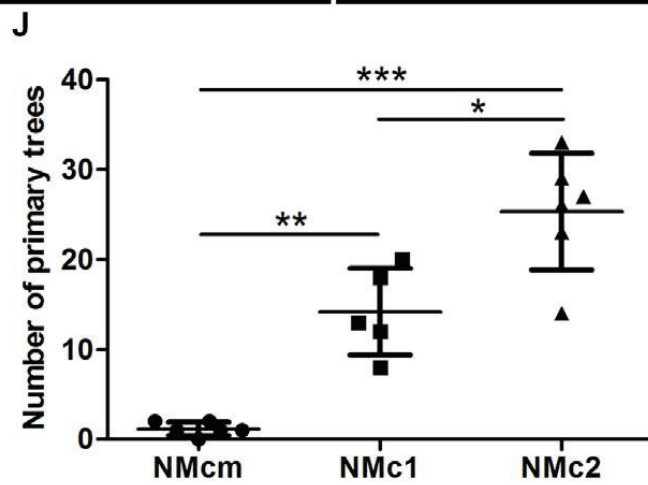
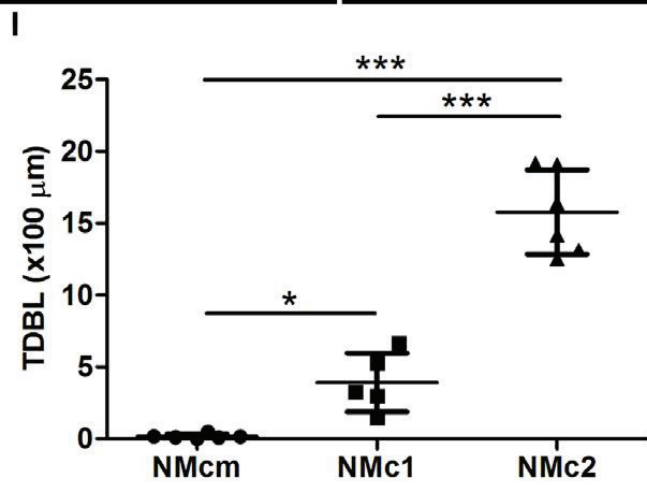
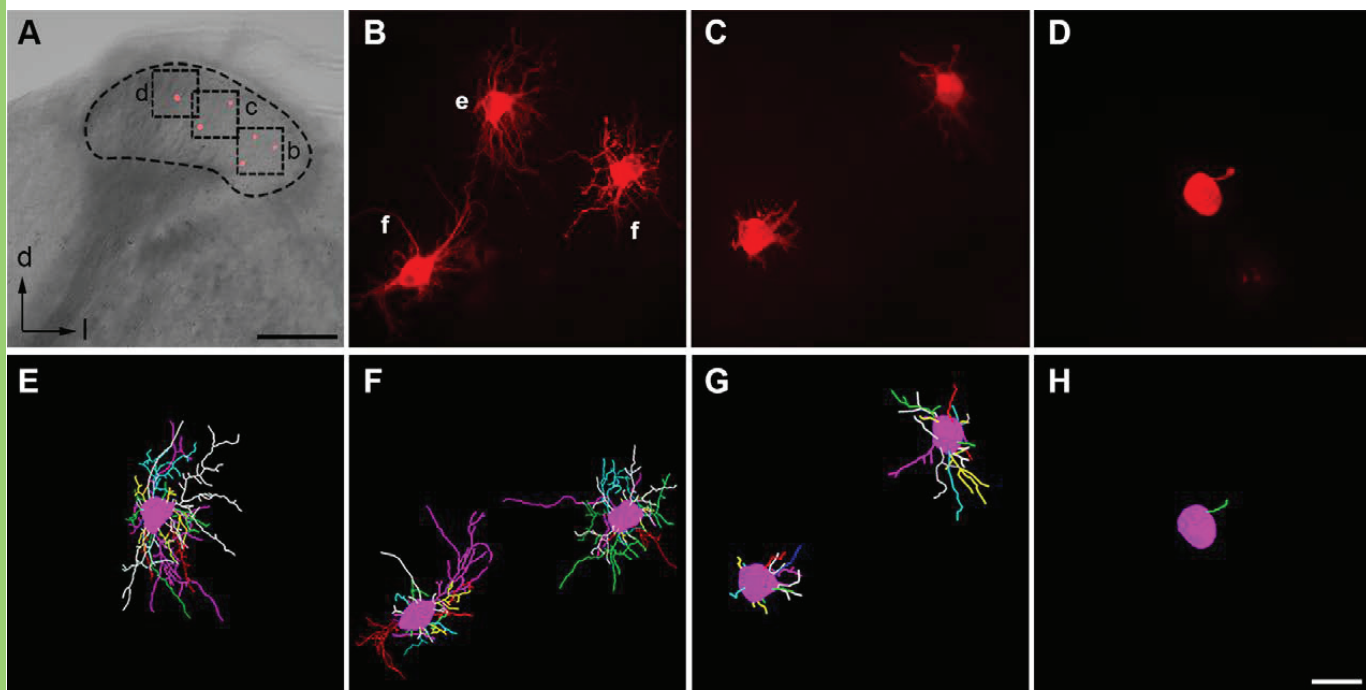
1380

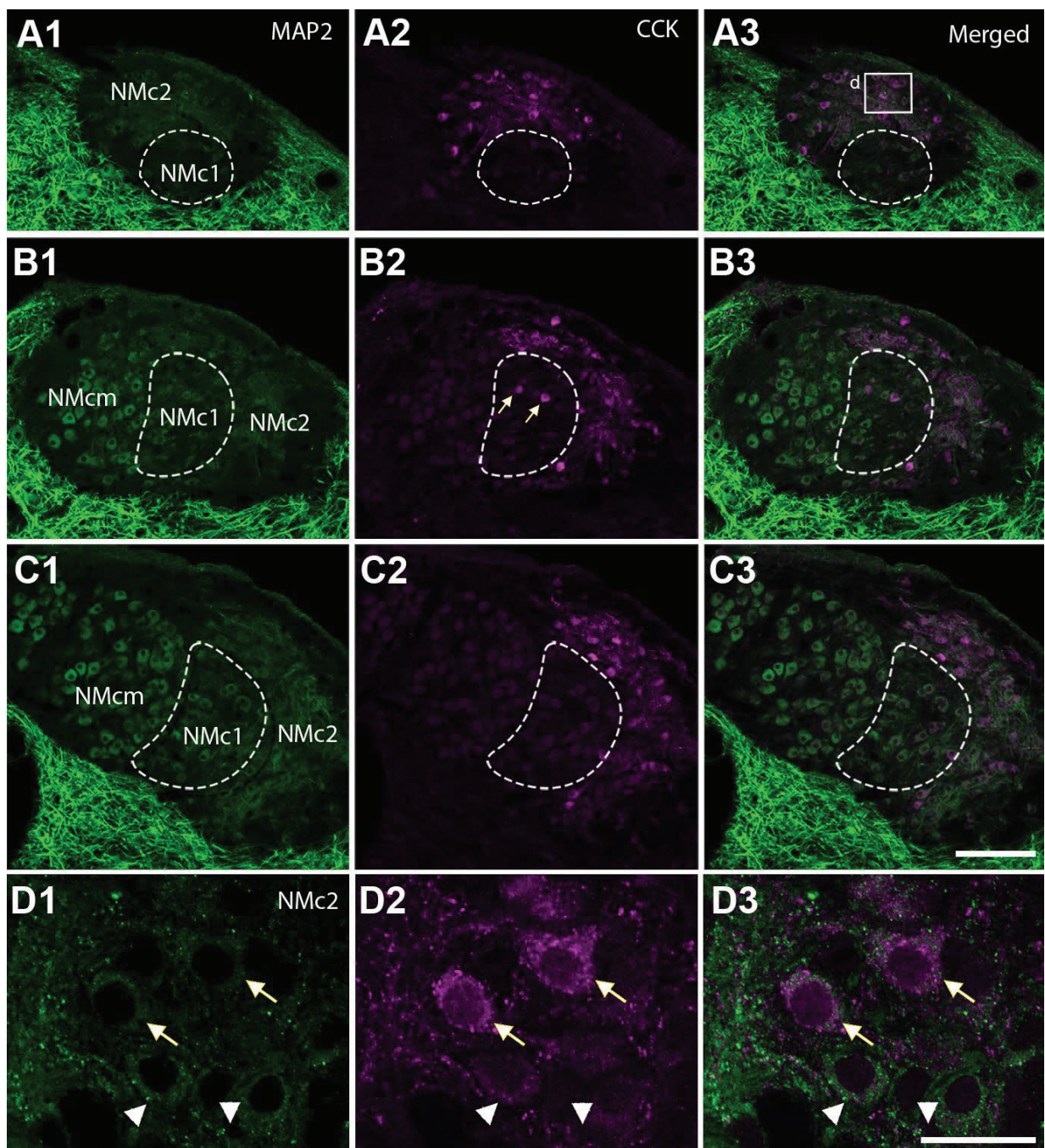
1381 **Figure 12: Summary drawings of neuronal features in caudal NM.** Based on
1382 cytoarchitecture, the caudal NM (regions outlined by solid black lines) is divided into three
1383 subdivisions, NMcm, NMc1 and NMc2. Borders between subregions are indicated by dashed
1384 lines. Left is medial and up is dorsal. **A:** Morphology and molecular signatures. NMcm, NMc1
1385 and NMc2 neurons exhibit different dendritic complexity and cell body size. Compared to

1386 NMcm neurons with few dendrites, NMc1 and NMc2 neurons preserve more dendrites. Notably,
1387 NMc2 neurons show longer total dendritic branch lengths than NMc1. On average, NMcm are
1388 larger than NMc1 and NMc2 neurons in somatic size. And the majority of cells with the smallest
1389 cell body sizes are located in NMc2. Moreover, neurons in the three subregions also show
1390 distinct expression patterns of calretinin (magenta), PV (green) and CCK (blue). Most neurons in
1391 NMcm and NMc1 express calretinin, while neurons in NMc2 are not immunoreactive for this
1392 protein. A substantial number of NMc1 neurons co-express calretinin and PV (half green and
1393 half magenta), but only few neurons in NMcm and NMc2 show PV expression. Whether CCK-
1394 positive neurons in NMc2 are immunoreactive for PV or calretinin is not determined. Blue
1395 circles only represent CCK immunoreactivity of NMc2 neurons, not indicating restricted
1396 expression in cell bodies. Extensive neuropil staining of PV (short green lines) is observed in all
1397 three subregions. In NMcm, PV neuropil staining show perisomatic pattern (green rings), while
1398 in NMc1 and NMc2, PV positive neuropils (green spots) scatter between cell bodies. **B:**
1399 Connectivity. Neurons in NMcm receive excitatory (blue) and inhibitory (orange) inputs via
1400 endbulbs and small boutons respectively. The inhibitory inputs form bouton synapses on the cell
1401 bodies. In contrast, NMc1 and NMc2 neurons receive both excitatory and inhibitory inputs via
1402 bouton terminals, primarily in the neuropil (presumably dendrites). **C:** Biophysics. NMcm
1403 neurons generate single onset action potential in response to sustained depolarization, while
1404 NMc1/NMc2 neurons display the ability of generating multiple action potentials to
1405 suprathreshold sustained depolarization and are spontaneously active. Abbreviations: See Figure
1406 1 for anatomical terms. CR, calretinin; PV, parvalbumin; CCK, cholecystokinin.

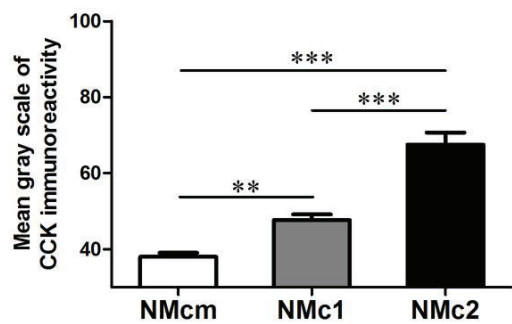




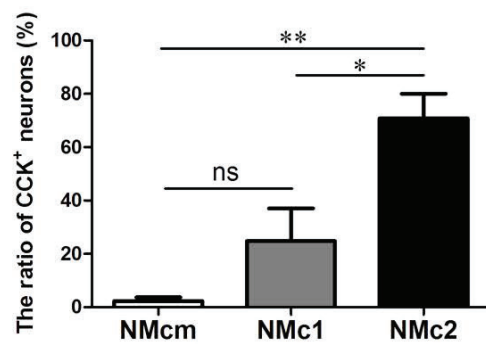


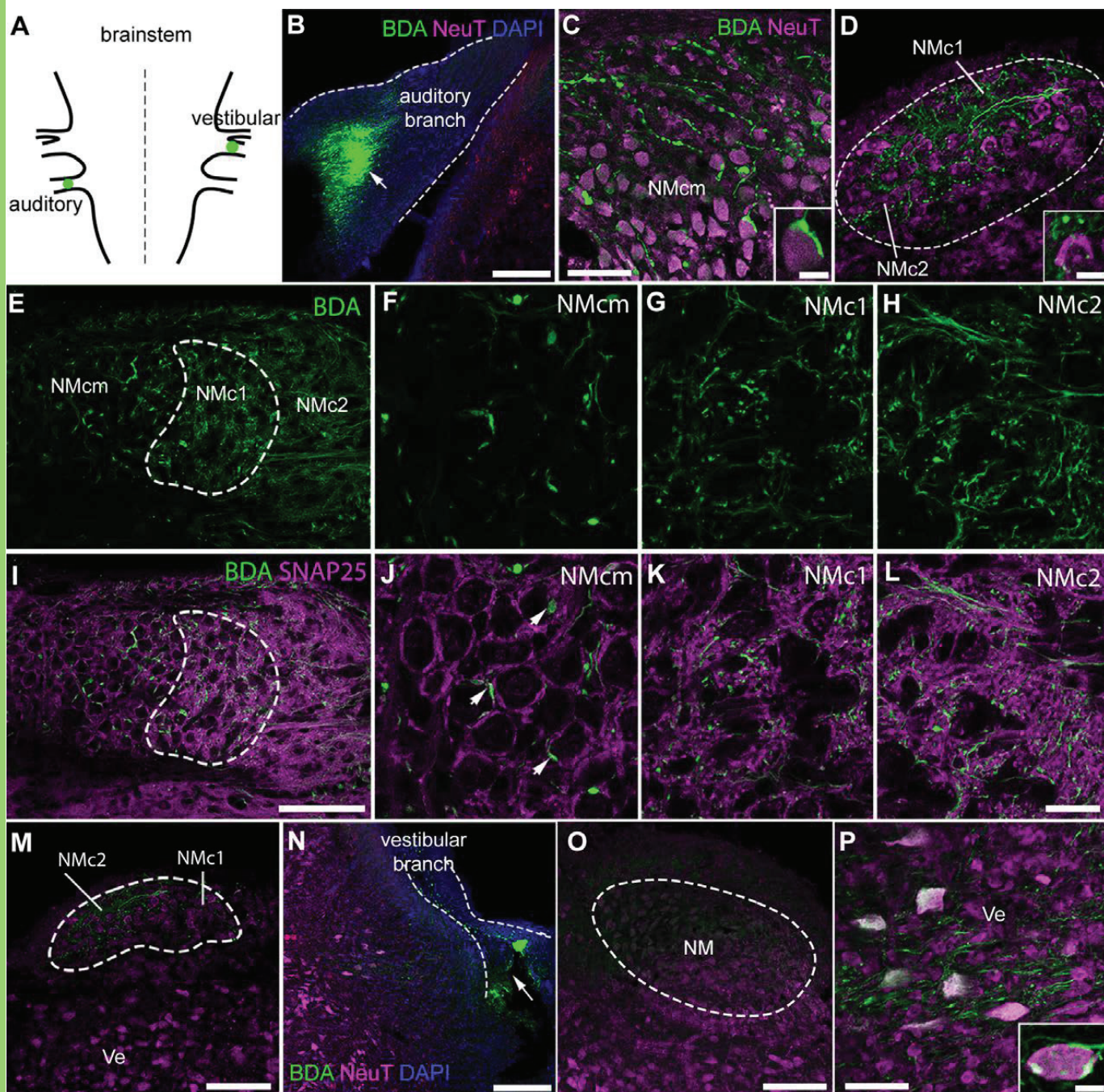


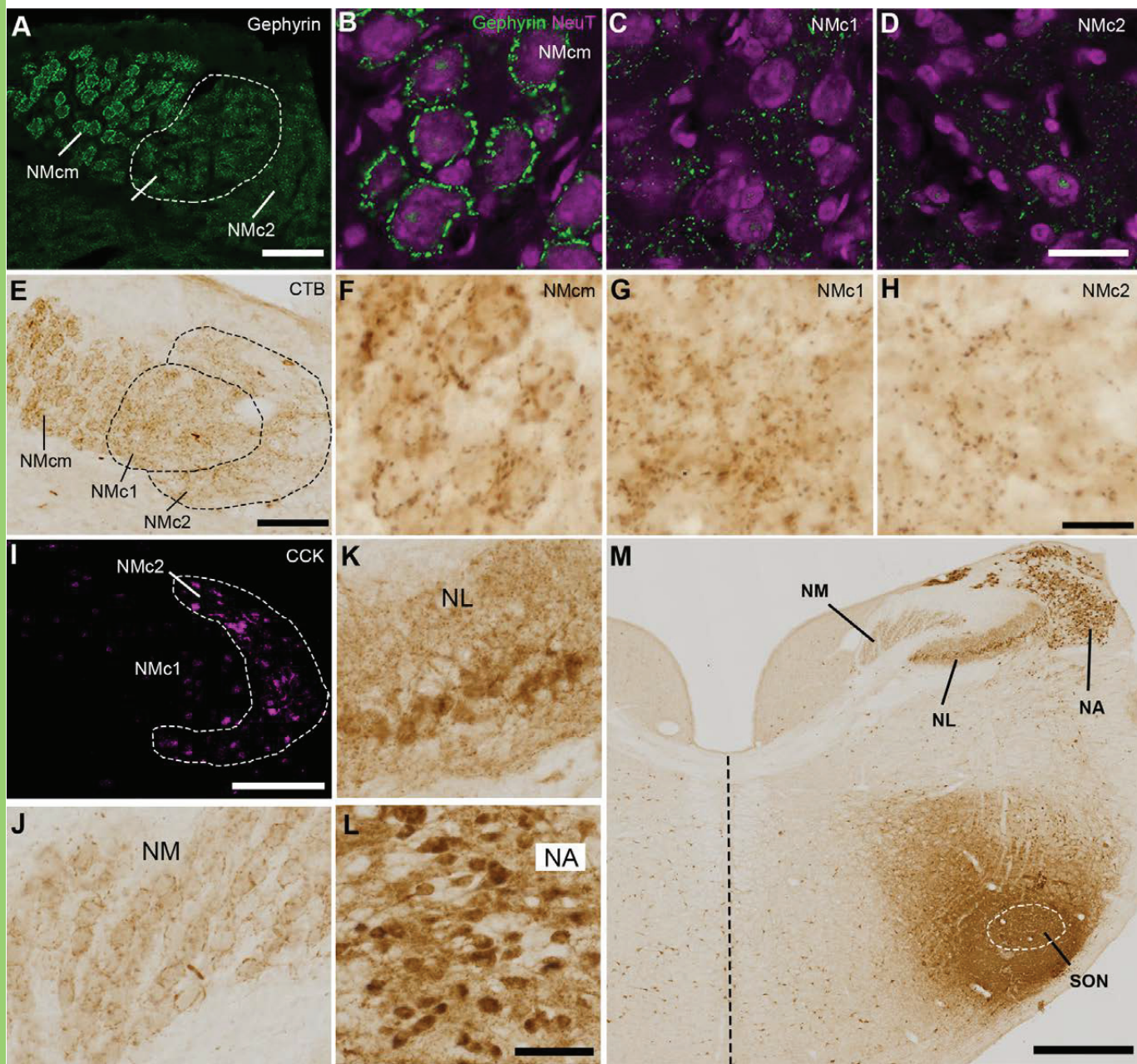
E

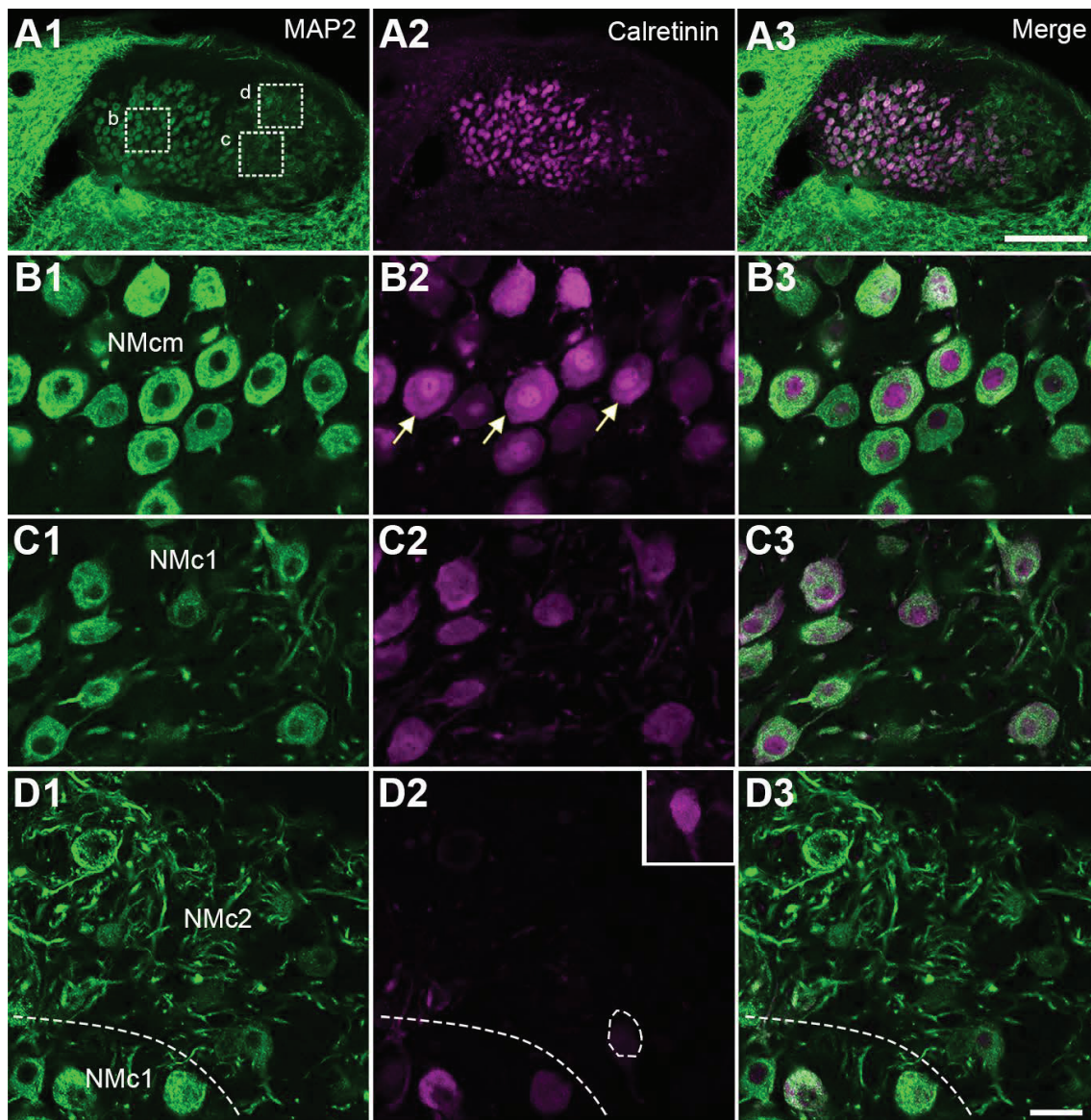


F









E

